Structure of photosystem II and substrate binding at room temperature

A full list of authors and affiliations appears at the end of the article.

[#] These authors contributed equally to this work.

Abstract

Light-induced oxidation of water by photosystem II (PS II) in plants, algae and cyanobacteria has generated most of the dioxygen in the atmosphere. PS II, a membrane-bound multi-subunit pigment-protein complex, couples the one-electron photochemistry at the reaction center with the four-electron redox chemistry of water oxidation at the Mn_4CaO_5 cluster in the oxygen-evolving complex (OEC) (Fig. 1a, Extended Data Fig. 1). Under illumination, the OEC cycles through five intermediate S-states (S_0 to S_4)[1], where S_1 is the dark stable state and S_3 is the last semi-stable state before O-O bond formation and O_2 evolution[2,3]. A detailed understanding of the O-O bond formation mechanism remains a challenge, and elucidating the structures of the OEC in the different S-states, as well as the binding of the two substrate waters to the catalytic site[4-6], is a prerequisite for this purpose. Here we report the use of femtosecond pulses from an X-ray free electron laser (XFEL) to obtain damage free, *room temperature* (RT) structures of dark-adapted (S_1), two-flash illuminated (2F; S_3-enriched), and ammonia-bound two-flash illuminated (2F-NH_3; S_3-enriched) PS II. Although the recent 1.95 Å structure of PS II[7] at *cryogenic temperature* using an XFEL provided a damage-free view of the S_1 state, RT measurements are required to study the structural landscape of proteins under functional conditions[8,9], and also for *in situ* advancement of the S-states. To investigate the water-binding site(s), ammonia, a water analog, has been used as a

marker, as it binds to the Mn_4CaO_5 cluster in the S_2 and S_3 states[10]. Since the ammonia-bound OEC is active, the ammonia-binding Mn site is not a substrate water site[10-13]. Thus, this approach, together with a comparison of the native dark and 2F states, is used to discriminate between proposed O-O bond formation mechanisms.

Diffraction to 2.0 Å (Fig. 1b) was observed at room temperature and structural datasets for the S_1 and the 2F states of PS II under different buffer conditions were obtained at 3.0 to 2.25 Å resolution (Methods, Extended Data Table 1, Supplementary Tables 1-4). The packing of the PS II dimers (Fig. 1c) and unit cell dimensions differ significantly from those from Suga *et al.*[7] (Extended Data Fig. 1). For the illuminated data, the unit cell dimensions remained the same as for the S_1-state data, in contrast to a recent report[14] (see also ref.[15]). Examples of the electron densities (*2mF_o-DF_c* and *polder* bulk solvent-excluding omit maps, see Methods) for several structural groups are shown in Fig. 1d-f and Extended Data Fig. 2 for the S_1 state (3.0 Å resolution) and the 2F state, with and without ammonia (at 2.8 and 2.25 Å resolution, respectively).

Compared to the cryogenic S_1 XFEL structure[7], a large-scale rotation of the monomers relative to each other by ~0.6° in the dimeric complex is observed in our RT S_1 XFEL structure. Within each monomer, the locations and orientations of transmembrane helices (TMH) also differ, resulting in an expansion of each monomer within the membrane (Fig. 2a, Extended Data Fig. 3). Systematic elongation of the center-to-center distances between the cofactors of the electron transport chain by 0.1 to 0.4 Å (Fig. 2b, Extended Data Fig. 4a) and expansion of distances between adjacent chlorophyll (Chl) centers involved in energy transfer in the antennae (CP43, CP47) (Fig. 2c, Extended Data Fig. 4b-d, Supplementary Table 5) by 1-3.5% (0.3-0.9 Å) compared to the cryogenic S_1 XFEL structure are observed. Changes of this magnitude are larger than the errors for the cofactors in our structure (Methods, Supplementary Table 5). Comparison of our RT S_1 XFEL structure with the cryogenic S_1 XFEL structure[7] and the cryogenic S_1 synchrotron radiation (SR) structure by Hellmich *et al.*[16] featuring a dimer packing similar to our RT XFEL structure (Extended Data Figs. 3,4, Supplementary Text) reveals that the majority of changes in TMH positions and cofactor distances are the result of the difference in data collection temperatures. Differences in the equilibrium distances have a profound influence on the calculated electron and excitation transfer rates in PS II. For example, extension of the $Pheo_{D1}$-Q_A distance by 0.2 Å leads to a reduction of calculated electron transfer rates[17] by ~25% and elongation of the distance between connecting Chls of the antennae and RC pigments from 20.5 to 20.9 Å yields a reduction in excitation transfer rates[18] by ~10%.

The RT structure exhibits an increase of ~50% in altered rotamers of side-chains relative to the differences between the cryogenic XFEL and SR structures (Fig. 2d, e), indicating that the rotamer distribution is affected by temperature, as observed for other proteins[8]. These differences are observed nearly exclusively in solvent-exposed regions of the complex (Fig. 2d), and they can be explained by (a) high flexibility of the residues at RT leading to no or only weak electron density; (b) the presence of multiple conformers at RT (*e.g.* Arg B476 in Fig. 2e); or (c) stabilization of a different conformer at RT (*e.g.* Phe B479 in Fig. 2e).

In our RT S_1 and 2F-NH$_3$ XFEL structures (3.0 and 2.8 Å resolution) ~120 waters per dimer were resolved, with omit maps indicating the presence of additional waters (Methods, Extended Data Fig. 5, Supplementary Table 6). In the higher-resolution native 2F RT XFEL structure, ~1200 waters were observed. The observation of key water molecules linking the OEC to possible proton channels[19] in our RT data (Extended Data Fig. 5) indicates that the channels postulated based on cryogenic structures[7,19] may be relevant in PS II under physiological conditions.

Electron density maps for the OEC are shown in Fig. 3a,b and Extended Data Fig. 6 for the S_1 (3.0 Å) and 2F data (2.25 Å). To minimize model bias, metal-metal distances in the OEC (Fig. 3c) were calculated from individual metal omit maps. The similarity of the distances in the S_1 RT structure with those in the cryogenic S_1 XFEL structure[7] (error estimates in Methods) confirms that the observed metal arrangement at 100 K[7] is valid for the physiological S_1 state at RT. While determining bridging oxygen positions is challenging in multimetallic clusters like the OEC as the electron density of the oxygens tends to be overwhelmed by the nearby metal density, oxygen positions modeled in the RT S_1 state match well with those of the cryogenic S_1 XFEL structure. Based on the Mn4-O5 (~2.3 Å) and Mn1-O5 (~2.7 Å) distances, however, we concluded, as suggested by X-ray spectroscopy[3], EPR[20] and theory[21], that O5 (Fig. 3a) is bound to the Mn4 site, but not bound to Mn1 in the S_1 state. This leads to an open cubane structure for the Mn$_4$CaO$_5$ unit.

In situ illumination of dark-adapted crystals at RT led to the formation of 2F crystals in which the S_3 state was predominant (Methods, Extended Data Fig. 7). In the 2F RT XFEL data, the cluster maintains its open cubane motif (Fig. 3b,c, Extended Data Fig. 6b), but changes are observed in some of the atomic positions, like O4 and Mn4. The Mn3-Mn4 distance is shortened by ~0.1 Å accompanied by a twist of the Mn3-O4-Mn4-O5 plane in relation to the Mn1-Mn2-Mn3 core structure (Fig. 3d). While a distance uncertainty of 0.10 to 0.15 Å remains at 2.25 Å resolution, the trend in metal-metal distance changes does not support S_3 models based on closed cube geometries (*e.g.* Extended Data Fig. 8a,d)[22] that require >0.5 Å elongation of Mn3-Mn4 or compression of Mn1-Mn3 distances. Similarly, our data do not support models in which a new water/hydroxo binds to Mn1 (Extended Data Fig. 8b)[20,21] as no corresponding electron density or distance changes were observed (Fig. 3e,f, Extended Data Fig. 6b).

All four water ligands to the OEC (W1–W4, Extended Data Fig. 1a) were clearly visible in our S_3-enriched 2F RT XFEL data, within 0.2-0.4 Å of their positions in the cryogenic S_1 XFEL structure; for example, W3 is displaced towards Glu189 and W4 towards Asp170 (Fig. 3b,d, Extended Data Fig. 5e, note that the W3 position in our RT S_1 structure is shifted by ~0.8 Å from the cryogenic S_1 XFEL structure, Extended Data Fig. 5d). No additional water/hydroxo ligand to the OEC was observed in the 2F data. Comparison of the ~20 waters within 7 Å of the OEC indicated that three of the 2nd sphere waters from the cryogenic S_1 XFEL structure, A571, A588 and C665, could not be located in the 2F structure, likely due to their mobility at RT or changes of the water arrangement around the OEC upon formation of the S_3 state (Extended Data Fig. 5e).

There are no large movements of the side chains surrounding the OEC, *e.g.* Asp 61, Asp 170 and Val 185 of D1, between the dark and native 2F structures (Fig. 3a,b,d) of the sort predicted in previous studies[14,23]. Instead, small movements on the order of 0.3 Å were noticeable in several side chains, in agreement with the data of Kern *et al.*[24].

At the electron-acceptor site no large differences are observed for the mobile quinone Q_B between the dark and native 2F structures. This is in line with the expectation that after two flashes Q_BH_2 is released and the Q_B pocket is filled with a new plastoquinone within the 500 ms period prior to sampling with the XFEL pulse (Extended Data Fig. 7a,b).

Insight into which of the water or hydroxo ligands of the Mn_4CaO_5 cluster are the substrate waters can be obtained by analyzing differences induced by ammonia binding (see Supplementary Text). Ammonia is known to bind to the Mn_4CaO_5 cluster at a non-substrate water binding site only upon illumination[10]. We thus obtained 2F RT XFEL data at pH 7.5 (2F-NH_3, 2.8 Å resolution) in the presence of 100 mM $(NH_4)_2SO_4$, and compared it with the native 2F data. In the 2F-NH_3 structure, about 75% of PS II centers are in either the S_2 or the S_3 state (Methods and Extended Data Fig. 7f-i). Ammonia binding to Mn was confirmed by the altered S_2 EPR multiline signal (Extended Data Fig. 7d,e)[25]. Although the Cl^--binding site was reported as a second, possibly inhibitory ammonia binding site (see Supplementary Text), we can exclude substitution of Cl^- by ammonia in our samples based on oxygen-evolution activity (Extended Data Fig. 7f-i) and inspection of the electron density (Extended Data Fig. 9a,b). Since a direct distinction between NH_3 and H_2O cannot be drawn from the data, we examined the structure around possible binding sites in the 2F-NH_3 data in comparison with the native 2F structure.

One of the proposed ammonia-binding sites is the μ-oxo bridging ligand O5 (Fig. 4a). Elongation of the Mn3–Mn4 distance is expected upon replacement of a μ-oxo bridge with an amido or imido-bridge[11] or a significant alteration of the core structure[26], *e.g.* changing from a di-μ-oxo to a mono-μ-oxo interaction upon loss of the Mn3-O5-Mn4 μ-oxo bridge. No such elongation was observed in the 2F-NH_3 data and therefore we eliminate this possibility, in agreement with EPR data[12]. Alternatively, ammonia could replace a terminal water ligand on Mn4, *i.e.* W1 or W2 (Fig. 4a), with W1 being favored based on the interpretation of EPR data[12,13]. The W1 position in the 2F-NH_3 data is very similar to that in the native 2F structure, while the placement of W2 reveals a shift of its position (Fig. 4b, Extended Data Fig. 9). Of the waters hydrogen-bonded to W2, H_2O^A (Fig. 4b) is in a position similar to the native 2F and the cryogenic S_1 XFEL structures, while H_2O^B is less well defined. A larger tilt of the W3 and W4 axis is also visible in the 2F-NH_3 data, as compared with the native 2F data. We note that the native 2F data were obtained by lowering the pH from 7.5 to 6.5; thus an alternative explanation of the observed change in the W2 site is that W2 is a hydroxide at pH 7.5, while it is fully protonated at pH 6.5.

Modeling the binding of NH_3 in place of W1 in the S_2-state[12,27] predicted either changes in the Mn3-Mn4 distance by 0.4 Å and displacement of the ammonia nitrogen with respect to the W1 position by about 1 Å[27] or ammonia at a position very similar to W1 in the Suga structure with minimal changes in the Mn3-Mn4 distance and a small movement of W2.[12] As our data do not show elongation of the Mn3-Mn4 distance, a scenario as postulated in

ref.[27] is unlikely. This leaves two options for NH_3-binding in the S_3 state, either at W1 with only minimal changes in the metal positions and ligand environment or at W2 (Fig. 4a).

W2 is less integrated in a strong hydrogen-bonding network compared to W1 (as also seen in ref.[7]), suggesting easier exchange of W2 if bound as fully protonated H_2O. On the other hand, the weaker H-bonding makes ammonia binding at the W2 site difficult to reconcile with the highly anisotropic nuclear quadrupole parameter of the bound ammonia[13]. We note that our data do not exclude ammonia moving from the W1 to W2 site or detaching from Mn during the $S_2 \rightarrow S_3$ transition[27,28].

Ammonia binding does not significantly affect the substrate water exchange rates in the S_2 and S_3 states (Extended Data Fig. 7)[10,12]. Therefore, if the structural change at W2 is caused, directly or indirectly, by ammonia binding, then W2 is not a likely substrate binding site in the S_3-state. In the context of the proposed mechanisms (Fig. 4c),[4,29-31] this would disfavor O-O bond formation via nucleophilic attack from Ca-bound W3 onto W2 (Fig. 4c(i)) and other mechanisms that use W2 (*e.g.* Fig. 4c(ii)). Since we did not find evidence for the presence of an additional water/hydroxo near Mn1 in the 2F samples, our data do not support direct coupling between a newly bound water-derived ligand on Mn1 and O5 (Fig. 4c(iii); see also ref.[2]). This leaves possible mechanisms such as O-O bond formation between W3 and O5 (Fig. 4c(iv)), between W1 and O4 (Fig. 4c(v)), or other mechanisms not involving W2 or an inserted water at Mn1.

Methods

Sample preparation

PS II dimers from *Thermosynechococcus (T.) elongatus* were prepared using a modification of the protocol described in Kern *et al.* (2005)[32], substituting the $C_{12}E_8$ detergent for β-DM and using betaine as a cryoprotectant instead of glycerol[16]. Crystallization was achieved by addition of PEG 5000 and seeding methods[33] to obtain a uniform size distribution of 5-15 μm for the MESH (microfluidic electrokinetic sample holder) injector (CXI instrument at LCLS) and 20-50 μm for the ADE (Acoustic Droplet Ejection)-DOT (Droplet on Tape) injector (XPP and MFX instruments at LCLS) (see **Sample Injection and Illumination**). Crystals were dehydrated by treatment with high concentrations of PEG 5000 before measurement. The final buffer used for the XRD measurements for the CXI instrument was 100 mM TRIS-Cl, pH 7.5, 100 mM $(NH_4)_2SO_4$, 31.5% (w/v) PEG 5000, 10% ethylene glycol. This procedure resulted in a change in unit cell parameters of the crystals compared to earlier crystallization protocols due to differences in crystal packing. The packing obtained from this procedure[16] is very similar to the arrangement of PS II dimers in the native thylakoid membrane of *T. elongatus*. The final buffer used for the XRD measurements for the XPP and MFX instruments was 100 mM MES pH 6.5, 100 mM ammonium chloride, 10 % ethylene glycol and 35% (w/v) PEG 5000. The same crystal packing as for the above-mentioned crystals was observed. Small differences in the unit cell parameters exist due to the different buffer condition and dehydration procedure.

Characterization of ammonia-treated PS II and establishing the preparation protocol—Prolonged incubation of PS II samples at higher pH, and with ammonia and

TRIS, are known to reduce the PS II oxygen evolution activity. For this reason, thorough control experiments were undertaken to characterize the light-induced turnover of purified PS II dimers under crystallization conditions in comparison to conditions at lower pH and without ammonia or TRIS addition. The buffers used were A (100 mM MES, pH 6.0, 10 mM $CaCl_2$, 30% glycerol) for low pH conditions, B (100 mM TRIS-Cl, pH 7.5, 100 mM $(NH_4)_2SO_4$, 30% glycerol) to mimic crystallization conditions in solution samples, C (100 mM TRIS-Cl, pH 7.5, 100 mM $(NH_4)_2SO_4$, 31.5% PEG 5000, 10% ethylene glycol) for measurements on crystals and D (100 mM TRIS-Cl, pH 7.5, 10 mM $CaCl_2$, 30% glycerol) for measurements at high pH without ammonia. EPR measurement of the content of Mn^{2+} released from crystals after 12 h incubation in buffer C yielded an upper bound of 5%.

O_2 activity—Measurement of the O_2 yield by means of a Clark-type electrode from crystals under continuous illumination showed 70-75% of the activity observed under low pH conditions (pH 6.0). To see if this reduction in activity is due to the pH effect or due to some fraction of Cl-binding sites being substituted with ammonia, we compared the O_2 activity of PS II in Buffer A (pH 6.0, no ammonia), in Buffer B (pH 7.5 with ammonia), and in Buffer D (pH 7.5, $CaCl_2$, no ammonia). The O_2 evolution rates of PS II in Buffer B and in Buffer D are similar and are 70% of the activity in Buffer A ($\approx$ 3000 μmol O_2/(mg(Chl) × h) with PPBQ and 3600 μmol O_2/(mg(Chl) × h) with DCBQ). Therefore, we conclude that the reduction of the O_2 activity in our ammonia-treated PS II is an effect of the higher pH. Similar results were obtained by Joliot-type O_2 oxygen evolution measurements (no electron acceptors added, 2 Hz flash frequency, Xe-flash lamp) on the same type of PS II core preparations (Extended Data Fig. 7, f-i). These experiments revealed similar O_2 oscillation pattern and comparable total O_2 yields with and without ammonia or TRIS or MOPS buffer at pH 7.5, even if incubated for several hours. One exception was that the total O_2 yield of the sample in buffer containing 100 mM $(NH_4)_2SO_4$ was 30% smaller than when suspended in buffer containing 100 mM Na_2SO_4. The data also show that our core preparations have a large enough plastoquinone pool to allow a full cycle of O_2 production in absence of added electron acceptors (Extended Data Fig. 7a). This was further confirmed by membrane-inlet mass spectrometry experiments where at very low frequency (12 s between flashes) an increase in O_2 yield of only 15% was observed if PPBQ was added (Extended Data Fig. 7b). The experiments were performed and analyzed as described earlier[34].

Importantly, nearly full activity (O_2 rates) can be restored in solution samples upon exchanging the sample back into pH 6.5 buffer, but keeping the $(NH_4)_2SO_4$ concentration constant. This implies that the OEC remains intact and that the lower overall activity at the higher pH may be associated with changes in the protonation state of residues involved in proton transfer networks around the OEC.

Electron density of the Cl-binding site—As described above, ammonia does not bind to the chloride-binding site(s) in the presence of excess chloride (100 mM) in PS II, and the O_2 activity results support this conclusion. To further confirm this, we checked the occupation of the two chloride-binding sites in the electron density map of the 2F data. As shown in Extended Data Fig. 9a,b, both sites are occupied by chloride. We have also checked this by substituting chloride with ammonia in the structural model and calculating

electron density difference maps using this substituted model after three cycles of refinement in *phenix.refine*. The appearance of positive difference density upon substitution confirmed that the density observed at both chloride-binding sites in the electron density maps from our dark and 2F data cannot be explained by ammonia (Extended Data Fig. 9 a,b). In summary, we can conclude that ammonia does not bind to the chloride-binding sites under the current experimental conditions.

EPR spectra of ammonia-treated PS II—Previous studies suggest that ammonia binds upon formation of the S_2 state and stays bound in the S_2-S_3 transition[10]. Therefore, we use the well-characterized S_2 EPR multiline signal (MLS) to infer the extent of ammonia binding in our 2F samples. The binding of ammonia to Mn in the S_2 state was confirmed by the altered EPR multiline spectrum. We measured EPR from both single flash (data not shown) and continuous illumination conditions with and without annealing to populate the S_2 state. These different procedures yielded similar results and for comparison with literature data we show here the spectra obtained using continuous illumination and annealing (Extended Data Fig. 7d,e). We compared the native PS II EPR multiline spectrum of the S_2 state (pH 6.0, no ammonia), the native PS II EPR multiline spectrum of the S_2 state (pH 7.5, no ammonia), and the ammonia-treated S_2 state spectrum (pH 7.5 in the presence of 100 mM ammonia). The spectral changes observed in the ammonia-treated S_2 state sample were similar to results reported previously[13,35] and the altered MLS was observed. Comparing spectral heights between the altered and native MLS is challenging as the peaks do not clearly correspond to each other. Nevertheless, when we assume that the MLS intensity of normal PS II (pH 7.5 without ammonia) and the altered MLS of ammonia-bound PS II (pH 7.5 with ammonia) both similarly reflect the number of unpaired spins, we estimate the altered MLS intensity to be ~70% of that of the normal PS II (calculated by the averaged peak heights of multiple EPR peaks at the high field side of the Y_D signal). The reduction in the MLS gives the lower limit for centers in the S_2 state as it could also be that, under elevated pH conditions, a fraction of the centers in the S_2 state do not give a MLS[36].

Determination of the S_3 state population in the native and ammonia-treated PS II 2F state—Flash-induced oxygen measurements in a replica of the capillary setup used in the XRD experiment were performed using membrane inlet mass spectrometry (MIMS) for O_2 detection[24,37,38]. Analysis of the flash data obtained for PS II crystals incubated for 12 h in buffer C (Extended Data Fig. 7f) showed that 50-60% of the centers active in oxygen evolution are in the S_3 state after two light flashes in the ammonia-treated PS II. We therefore conclude that in the 2F ammonia-treated PS II samples, S_3 is formed in 50-60% of the centers, with most of the remaining centers (~25%) being in the S_2 state. Therefore, 75%-85% of the centers are expected to bind ammonia in the 2F samples. This estimate was confirmed with the independent Joliot-type flash-induced oxygen evolution measurements on solution samples of our PS II core complexes. The analysis of these patterns (Extended Data Fig. 7 g-i) gives an S_3 state population of about 53% in the 2F samples at pH 7.5 (TRIS, $(NH_4)_2SO_4$), and of 60% at pH 6.5 (MES, $(NH_4)_2SO_4$) (Extended Data Fig. 7a, g-i).

At pH 7.5 the O_2 evolution rate is reversibly reduced to 70-75% of its maximum value at pH 6.0, and the MLS amplitude is reduced to a similar extent (Extended Data Fig. 7d). Similarly, the total O_2 yield obtained in flash-induced oxygen evolution pattern was about 50% at pH 7.6 compared to 6.5. Since we do not know with certainty whether these reductions are due to reversible blockage of centers in a particular S-state or due to kinetic limitations (O_2) or changes in the hyperfine couplings (EPR)[36], some uncertainty arises as to the S-state population of the 2F-NH_3 samples when normalized to all centers. Therefore, the most conservative estimate for the S-state distribution in the current 2F-NH_3 crystals is 25% S_3 state. In contrast, the highest estimate of the S_3 state occupancy in the 2F-NH_3 sample becomes 50%, with 25% in the S_2 state.

Sample injection and illumination

Crystals in high PEG 5000 buffer (31.5% w/v) were injected using a modified version of the electrospinning injector (MESH) of Sierra *et al.*[39]. In the modified version, a double capillary setup was used, allowing the protection of the crystals in mother liquor with a shield flow of 50% ethylene glycol. The setup is discussed in detail in Sierra *et al.*[40]. Illumination of samples was performed as described previously[24] and optimal illumination parameters were established by parallel oxygen yield measurements using MIMS (Extended Data Fig. 7b,c,f). The experimental setup at the CXI instrument[47] of LCLS was similar to the one used in our previous work[26,48]. For the ammonia-treated doubly illuminated (2F-NH_3) data each volume segment of the crystal suspension was illuminated by 120 ns laser pulses (20 ± 2 mJ/cm^2) at 527 nm from lasers 2 and 3 along the sample delivery capillary, resulting in a delay time of 0.5 s between the 1st and 2nd illumination and of 0.5 s between the 2nd illumination and the X-ray probe.

For the high-resolution 2F structure of the native PS II, the data was collected at the XPP and the MFX instruments of LCLS[41,42]. The newly developed Drop-on-Tape (DOT) sample delivery method was used in combination with an acoustic droplet ejection (ADE) method[43]. The laser illumination timing remains the same as that used for MESH, using 100 ns laser pulses at 527 nm from a Nd:YLF laser (Evolution, Coherent). For testing light saturation for the DOT system, a 100-150 μm film was established with the help of a washer between the silicon membrane of the mass spectrometer inlet and a thin microscope glass plate ('thin layer MIMS setup'). In this test setup the samples were illuminated with a pulsed Nd YAG laser (532 nm, Continuum). The laser energy was measured at the sample position. To allow resolution of the individual O_2 yields (Yn; n = flash number), the flashes had to be spaced by 12 s, which leads to a significantly lower Y3/Y4 ratio (Extended Data Fig. 7b) than at 2 Hz used in the Joliot-type experiments (Extended data Fig. 7a,g-i) and during the XFEL measurements. The data in Extended Data Fig. 7c show that the samples are saturated at 70 mJ/cm^2. At the XFEL a light intensity of 120 ± 10 mJ/cm^2 was applied.

X-ray diffraction setup and data processing

PS II XRD data collected at the CXI instrument[44] of LCLS were recorded on a CSPAD detector operating at a frame rate of 120 Hz, over an aggregate total time period of 641 minutes, and processed using *cctbx.xfel*[45,46]. To avoid saturating pixels on the CSPAD, which has a limited dynamic range of ~350 photons/pixel at 8 keV in its high gain mode[47],

we used the CSPAD detector in a 'mixed gain' mode, putting the low resolution pixels in a low-gain setting while the high resolution pixels were set to high gain. The low-gain mode is less sensitive to low signal but harder to saturate, thus preserving bright, low resolution reflections. Conversely, the high-gain setting is easier to saturate, but is more sensitive to low signal, as is typical for high resolution reflections. After subtracting a pedestal estimate derived from an uncorrected, dark average, we applied a gain multiplier of 6.88 to the pixels in the low-gain setting, thereby putting low- and high-gain pixels on a similar scale. This number is merely an estimate based on matching the background levels at the low/high gain boundary. A more thorough exploration of gain for protein diffraction data on the CSPAD detector is planned.

Thermolysin pseudo-powder patterns were generated by taking the maximum value of each pixel from the ensemble of diffraction patterns in a reference thermolysin data set[40] collected at a known detector distance. A precise sample-to-detector distance and the locations and orientations of the 64 sensors on the CSPAD X-ray diffraction detector were obtained by refining the geometries of the 64 sensors against all the single crystal models from the data set[46].

PS II XRD data collected at the XPP and the MFX instruments were recorded on a Rayonix detector operating at its maximum frame rate of 10 Hz in the 2-by-2 binning mode, in which square 'bins' of 4 pixels are configured to share underlying electronics and act as a single pixel. This mode was selected as a compromise between high data acquisition rates at larger effective pixel sizes and improved ability to resolve individual Bragg spots, especially for large unit cells, at smaller effective pixel sizes. In all binning modes, the dynamic range of the Rayonix detector is also larger than that of the CSPAD. Using this detector and the ADE-DOT sample delivery system, XRD data could be acquired from larger crystals (20-50 μm) than were used at the CXI instrument using the CSPAD and the modified MESH sample delivery system (5-15 μm).

Images were indexed using the Rossmann algorithm[48,49] as implemented in LABELIT[50], with the choice of lattice basis guided by a target unit cell of a=118.2 Å, b=224.6 Å, c=331.9 Å, a=β=γ=90° (later refined for data merging, Extended Data Table 1) for the dark and the 2F-NH$_3$ PS II data sets. This cell was determined by examining the distribution of unit cell dimensions found when indexing with no target unit cell. Indexing was attempted on all frames, without a pre-filtering step, so as to obtain the maximal number of indexed images. As previously described in detail[51] the Rossmann algorithm produces three basis vectors that generate a primitive triclinic lattice. Miller indices are then deduced for the strong spots, and the lattice parameters (unit cell and crystal orientation) are refined against the observed spot positions. Next, the lattice parameters are constrained to the known orthorhombic symmetry of the space group (in this case, P2$_1$2$_1$2$_1$), meaning the cell angles are all set to 90°, and the remaining free lattice parameters are re-refined. However, we noticed a potential problem with applying the orthorhombic constraints: we had previously redetermined the Miller indices of the strong spots based on their proximity to lattice nodes, after applying the 90° constraints. We found that this can sometimes assign Miller indices that are misindexed by one unit along the c axis, since the large ~332 Å cell length gives lattice nodes that are very close together. We therefore incorporated a new option within *cctbx.xfel* to apply high-

symmetry constraints, but skip the step of redetermining the Miller indices; instead, the initially-determined Miller indices are converted from the triclinic to the high-symmetry setting using a change-of-basis operator[52] before performing the final round of parameter refinement. Refinement was implemented using the newly introduced *DIALS* toolkit[53], which implements a target function based on both the observed spot positions and the reciprocal lattice points' angular proximity to the Ewald sphere[51], while also permitting the refinement of additional parameters such as the detector tilt. As in previous work[46], strong spots not covered by the modeled lattice were considered separately in an attempt to index a second lattice on each image for the dark and 2F-NH$_3$ data sets. We note that different unit cell parameters were obtained for the higher resolution 2F data of native PS II collected at the XPP and the MFX instruments. Using the ADE-DOT method and slightly different dehydration conditions, an average unit cell of a=117.9 Å, b=223.1 Å, c=310.7 Å, a=β=γ=90° was obtained, and a subsequent indexing step using these parameters as constraints was used to generate the final native PS II 2F dataset[43].

For the integration and merging of high-resolution reflections, we took into account various community concerns that weak reflections ought to be included since they contain measurable information[54], while at the same time realizing that shot-to-shot and crystal-to-crystal variation requires differing resolution cutoffs for each integrated image. For the work described here, the following solution was adopted: For each image, a first round of spot prediction and integration was performed, with a high-resolution cutoff based on the apparent limit of bright spots from the spotfinding program[55]. The intensity/standard deviation ratio ($I/\sigma(I)$) was examined as a function of diffraction angle to determine the resolution bin where $<I/\sigma(I)>$=0.5, essentially identifying a zone where the signal-to-noise falls to a low, but non-zero value. Then, for a second round of spot prediction and integration, the limiting resolution was set to a value far beyond the $<I/\sigma(I)>$=0.5 limit, in order to assure that any reasonable positive signal is integrated. This "greedy" integration limit was set to a reciprocal-spacing value that encloses 1.5 times the reciprocal-space volume as the limit determined by $<I/\sigma(I)>$=0.5.

Based on the integrated intensity measurements from this second round of integration, individual resolution limits were then determined for each image as follows: $<I/\sigma(I)>$ values were computed in resolution bins as a function of the diffraction angle, and the bins were excluded from further data merging beginning in the bin where $<I/\sigma(I)>$ first falls below 0.1. This threshold, which is essentially zero, implies that measurements beyond the limiting bin are half positive and half negative on average, suggesting that no actual Bragg signal is present.

Before scaling and merging the dark and 2F-NH$_3$ datasets, images with a refined c axis that was not between 325 and 340 Å were discarded. In the case of the native 2F dataset, the unit cell constraint during indexing ensured that no images with aberrant unit cells were integrated. Additionally, we examined the distribution of refined beam centers for all images. The beam center (indicating the relation between the detector and the incident X-rays) is freely refined during parameter refinement, even though the true relative positions of the beam and detector are fixed to within a micron. The small fraction of images whose beam center differed by more than one pixel from the mean were discarded, as these lattices

were mis-indexed by one Miller index unit along a crystallographic axis, usually the long *c* axis. As the unit cell lengths of this crystal form differ from those of other PS II crystal forms reported elsewhere[16], reference intensities for scaling were not available. We therefore merged and scaled the data initially without an external reference, using our postrefinement program *PRIME* recently described[56]. A resolution cutoff of 2.5 Å was chosen in this step to match the apparent resolution limit of the raw diffraction patterns. A total of 1264, 22311 and 2294 diffraction images were included in the S_1 state, native 2F and the 2F-NH_3 data sets, respectively (Supplementary Table 1). Following merging and post-refinement, complete data sets for the dark, native 2F and 2F-NH_3 states were obtained at 3.0, 2.25 and 2.8 Å resolution, respectively, and structural models were refined (see below for detailed description) to R_{work}/R_{free} of 0.2637/0.3030 for the dark, 0.1949/0.2308 for the 2F and 0.2497/0.2997 for the 2F-NH_3 state (Extended Data Table 1, Supplementary Tables 2-4).

For the dark and 2F-NH_3 data sets an initial model was determined with *Phaser* molecular replacement[57] using two copies of a hybrid model of the PS II monomer composed of the cryogenic S_1 state PS II structure from *T. vulcanus* ([7], PDB ID 4UB6) and the additional chain present in native PS II from *T. elongatus* ([16], PDB ID 4PJ0). The initial model was refined using *phenix.refine*[58] and used to calculate model structure factors, which were then used as a scaling reference to re-scale the original data using the program *cxi.merge*. For the native 2F data set the 2F-NH_3 model was used for *Phaser* molecular replacement. Examination of the I/σ(I) and completeness measures as a function of resolution allowed for selection of new resolution cutoffs at this stage and re-merging of the data with *cxi.merge* to these cutoffs. Negative measurements were included during merging instead of being discarded as had been done previously[46]. Generally, including negative measurements moves the distribution of merged intensities closer to that expected for crystallographic data, as measured using the L and Z tests[59] (results not shown). Further investigation of this effect is ongoing and will be the subject of a future work.

Custom restraints for the Mn_4CaO_5 complex geometry for the dark state complex, derived from the work of Suga *et al.*[7], were generated by averaging bond lengths and angles over the four crystallographically independent monomers in two structures (PDB IDs 4UB6, 4UB8) and imposing custom bond length and angle tolerances (see Supplementary Table 7 for restraints used). Average nonbonding distances between the cluster and surrounding residues were also calculated across the four monomers and adapted as restraints for the RT structures. Water molecules directly coordinating cluster metal atoms were restrained to match those in the Suga *et al.* structures in early cycles of refinement, and these restraints were subsequently modified to minimize difference density, resulting in separate sets of metal-water restraints for the two crystallographically nonequivalent PS II monomers. Custom restraints were also generated for the α- and β-pucker chlorophyll-a ligands in order to effectively restrain the planarity of the porphyrin ring, the magnitude of displacement of the Mg center from the plane of the ring, the direction of this displacement relative to the phytyl tail (which differs between α- and β-pucker stereoisomers), and the Mg-His or Mg-water coordination distances at this medium resolution. The chlorophyll restraints were based on the default chlorophyll-a (CLA) ligand CIF file distributed with *Phenix*[60]. In the higher-resolution native 2F dataset, the data quality was sufficient to generalize to a single chlorophyll-a restraints file for both α- and β-puckers, but restraints maintaining

coordination of chlorophyll magnesium atoms with nearby histidine sidechains or water molecules were still necessary to override the automatic repulsion of atoms within van der Waals distance of each other.

Model building and map calculation—Model building was performed in *Coot*[61] and figures were generated using *PyMol*[62]. Model building was aided by recently-developed tools: Feature-enhanced maps, designed to scale all non-solvent density to a uniform level, were used to identify highly flexible portions of ligands and detergent molecules once refinement had approached convergence[58]. *Polder* omit maps[63], a form of omit maps newly available with the *Phenix* package, were used to test the contribution of model bias to the observed electron density at selected ligands and TMHs and to identify unmodeled water molecules in the vicinity of the Mn_4CaO_5 cluster. *Polder* omit maps are able to reveal weaker features than traditional omit maps by uniformly omitting bulk solvent from the omitted region and its surroundings, a key advantage when locating ordered solvent. To test model bias, *polder* omit maps were calculated after perturbing the model with an area of interest omitted: the selected ligand or residues were omitted, the resulting model was subjected to three cycles of coordinate and real space refinement in *phenix.refine*, the omitted ligand or residues were re-inserted (to allow identification of the region from which to omit bulk solvent), and the *polder* omit map was calculated (once again omitting the selected atoms in addition to the surrounding bulk solvent). Simulated annealing *polder* omit maps were calculated identically but with simulated annealing enabled during coordinate refinement. A comparison of normal $mF_o\text{-}DF_c$ and *polder* omit maps with real space or simulated annealing is shown in Extended Data Fig. 2e-h. The advantage of the *polder* compared to the $mF_o\text{-}DF_c$ map is manifested in lower noise and higher levels of detail of the obtained electron density maps (*cf.* Extended Data Fig. 2g, h). Comparing simulated annealing and real space *polder* omit maps for several different regions in the PS II complex (*e.g.* Extended Data Fig. 2f, h) shows that both are very similar, with the simulated annealing being slightly more disruptive to the structure. As no additional benefit of the simulated annealing protocol was found all other *polder* omit maps shown in this work are generated after real space refinement of the omit model.

Modeling of waters—Waters were incorporated into the model in two different steps. After initial refinement of the model, waters were placed into the $2mF_o\text{-}DF_c$ map using the *Phenix* auto water placement option during several subsequent coordinate refinement cycles. These positions were manually checked in *Coot,* and waters with strong enough electron density and good hydrogen bonding environments were then included in subsequent runs of refinement of the model with auto water placement disabled and coordinate and real space refinement enabled, resulting in 124, 1179 and 107 ordered waters in the dark, 2F and 2F-NH_3 datasets, respectively (Extended Data Fig. 5). Upon convergence, *polder* omit maps excluding all waters were generated, and these were inspected for the placement of possible additional waters in the region around the OEC and within hydrogen bonding distance from hydrogen bonding-capable residues in the final model. For the two lower resolution data sets waters were placed manually into *polder* maps in *Coot* and their positions were fit to the density using the *Coot* rigid body fit tool. The resulting model was subsequently refined for three cycles in *phenix.refine* with coordinate and real space refinement enabled. This

resulted in an additional 33 and 55 water positions for the dark and 2F-NH$_3$ data sets, respectively (see *e.g.* Extended Data Fig. 5d). The coordinates for these additional waters are not included in the deposited PDB files but are given in Supplementary Table 6.

Estimated positional precision—To estimate the error when calculating differences in distances between cofactors, we sought to identify a method for determining the coordinate error of a molecule or residue sequence as a unit, for which the maximum likelihood estimate for atomic coordinate error (0.5 Å for our dark and 2F-NH$_3$ models, 0.34 Å for our native 2F model, 0.34 Å for 4PJ0 and 0.27 Å for 4UB6) is not a good guide. Instead we estimated the error in the positions of larger segments or molecules by generating simulated annealing omit maps of individual chlorophylls and TMHs. Treating the omitted unit as a rigid body, we obtained the best fit of the unit to *polder* difference density and calculated the magnitude of the shift as the distance between the center of the unit in the refined model and the center of the unit placed in the difference density. In the case of chlorophylls, the center was defined as the average of the positions of the four porphyrin nitrogens, and in the case of the TMHs, the average of the positions of all alpha carbons was used. Based on these results we estimate that we can position an entire Chl molecule with better than 0.13 Å precision in the dark model and 0.10 Å in the 2F and 2F-NH$_3$ model. Similarly for a TMH we arrive at an upper bound of 0.08 Å precision for all three models. It is expected that the positional error should approach the maximum likelihood estimate for atomic coordinate error as the size of the unit decreases. Using the same procedure, the non-heme Fe^{II} shifted by 0.5-0.8 Å in the dark model, 0.0 Å in the 2F model and 0.3-0.5 Å in the 2F-NH$_3$ model.

To estimate the precision in deriving the metal ion positions in the OEC, we compared a modification of the above technique and a difference-density generating technique. For the former, individual metal atoms were omitted from the cluster, but since *polder* maps are inapplicable when omitting single atoms from a larger molecule, standard mF_o-DF_c maps were used. Also, to prevent the collapse of coordinating waters into the cluster, waters coordinating Ca1 or Mn4 were omitted along with these atoms and restored to the annealed model prior to calculating mF_o-DF_c maps. The mobile W4, which was placed after refinement and is not included in the deposited model for the dark and 2F-NH$_3$ datasets, was also added to the annealed model before map calculation for Ca1 only, since the difference density at the Ca1 center was skewed in its absence. Observed shifts for each metal, averaged across the two monomers, ranged from 0.2 to 0.6 Å in the dark model, 0.1 to 0.6 Å in the 2F model and 0.2 to 0.4 Å in the 2F-NH$_3$ model. These values are likely overestimates due to the propensity for the whole cluster to shift into the open density during refinement and for the surrounding, coordinated waters to affect the difference density.

In the latter, we shifted individual metals in increments of 0.1 Å and calculated the resulting difference density (mF_o-DF_c). We propose that the magnitude of shift necessary to generate paired positive and negative difference density on either side of the atom can serve as an estimate of the positional error in OEC metal positions. A shift of Mn4 of 0.1 Å along the Mn4-Mn3 direction away from Mn3 led to paired difference density at the 2 σ contour level and a shift of 0.2 Å led to strong paired difference density at the 2.5 σ contour level in the lowest resolution dataset, clearly above the noise in the surrounding in the difference map. Combining the results from both approaches, we estimate the precision of our metal

positions to be in the range of 0.2-0.4 Å for the dark model, 0.1-0.3 Å for the 2F model and 0.2-0.3 Å for the 2F-NH$_3$ model.

## Comparison between the different PS II structures

Monomers or dimers of PS II from the 4UB6 and 4PJ0 models were superimposed onto our RT dark and 2F structural models using *Coot*. Cofactor distances were calculated as center-center distances. In the case of Chl and Pheo, the center is defined as the average of the positions of the four porphyrin nitrogens. For comparing distances of cofactors from the pseudo C2-axis the axis was defined as the membrane normal passing through the middle between the Pheo$_{D1}$ and Pheo$_{D2}$ molecules and distances of each pigment center from this axis were computed. For comparison of individual residue positions the models were aligned for short windows of 5-20 residues. For each of the two data sets, the quality of match between the *2mF$_o$-DF$_c$* maps (together with the refined models) and the 4PJ0 or the 4UB6 models was inspected visually and scored. For several residues clear difference density was visible in the initial rounds of model building when the starting model (based on the cryogenic structures) was used for generation of the electron density maps. Additional, *polder mF$_o$-DF$_c$* maps were used to inspect different rotamer conformations.
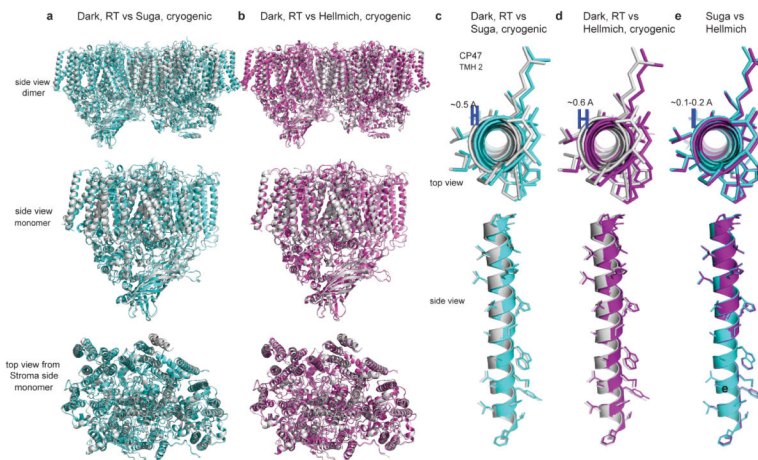
Extended Data
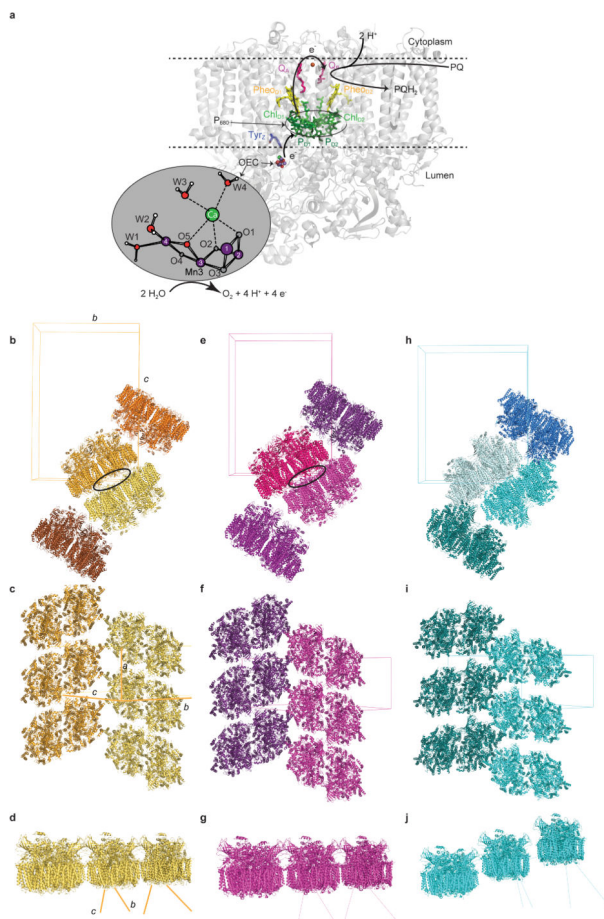
Extended Data Figure 1. Schematic of the reaction center and oxygen evolving complex (OEC) in PS II and packing of the dimeric complex in the crystal lattice

a) The reaction center is shown with cofactors labeled as Pheo: pheophytin; Chl: chlorophyll; PQ: plastoquinone; Q_A, Q_B: primary and secondary acceptor plastoquinones bound to PS II. The numbering of Mn (purple spheres), oxygen (red/grey spheres) atoms and metal-bound waters in the OEC follows the convention of Umena *et al*[21]. Upon illumination of PS II, an electron is transferred ~35 Å across the membrane from the excited primary electron donor P_{680} to the final electron acceptor Q_B via Chl_{D1}, pheophytin ($Pheo_{D1}$), Q_A, and a non-heme Fe^{II}. After accepting two electrons and undergoing protonation, plastoquinol Q_BH_2 is released from PS II into the membrane matrix. The photo-generated radical cation $P_{680}^{\bullet+}$ is reduced by a tyrosine residue (Tyr_Z) to generate a neutral tyrosine radical $Tyr_Z\bullet$, which acts as an oxidizing agent for water at the OEC. **b,c,d,** Packing of the dimeric complex observed in the RT data for three different view directions. The unit cell is indicated by a wire frame and axes are labeled. Dimers related by translation are colored identically. **e,f,g,** Packing observed in the cryogenic structure by Hellmich *et al.* (PDB: 4PJ0)[16] in the same orientations as in panels b,c,d. **h,i,j,** Packing observed in the cryogenic XFEL structure of Suga *et al.* (PDB: 4UB6)[7]. The space group is the same in all three cases, but the unit cell dimensions and packing are different. Whereas the *a* and *b* dimensions are very similar between 4PJ0 and the current RT data, the *c* axis is elongated. This results in a very similar arrangement of dimers in rows along the *a* axis (*cf.* **d** and **g**), whereas there is a larger spacing between two dimer rows at the cytoplasmic side of the complex (*cf.* black ellipse in **b** and **e**) due to the elongation of the *c* axis in the RT packing. The Suga structure[7] has a very different arrangement of the dimers and no closely packed rows of dimers are visible (*cf.* panels **c** and **f** compared with **i** and panels **d** and **g** compared with **j**).
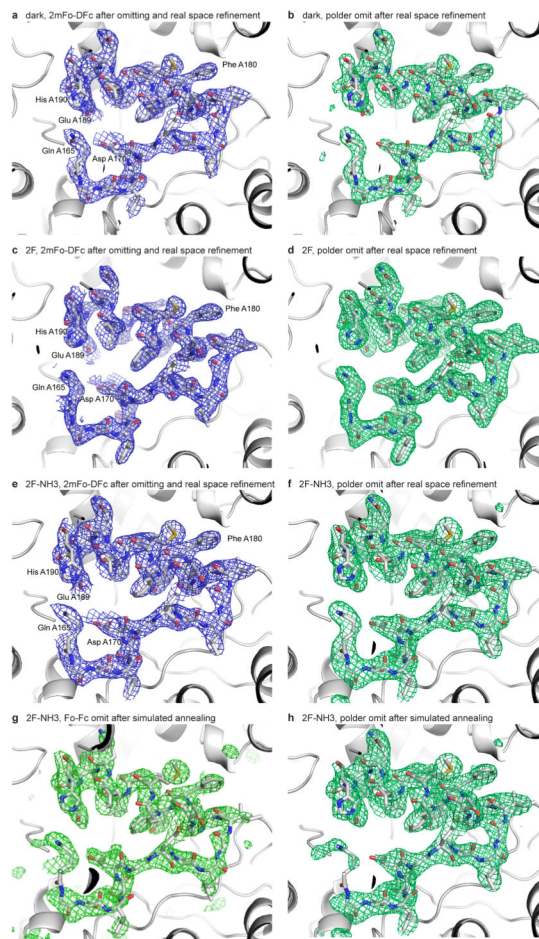
Extended Data Figure 2. Electron density omit maps of the lumenal CD helix and part of the loop region of subunit D1

Obtained from the RT dark (**a, b**), 2F (**c, d**), and 2F-NH$_3$ (**e-h**) data sets. For all maps residues 165-190 of subunit D1 (shown as grey sticks) were omitted followed by three rounds of coordinate and real space refinement of the model with (g, h) or without (a-f) simulated annealing in *phenix.refine*. **a,** *2mF$_o$-DF$_c$* map (blue, 1.5 σ contour) of the dark data set. **b,** *Polder mF$_o$-DF$_c$* map (green, 4 σ contour) of the dark data set. **c,** *2mF$_o$-DF$_c$* map (blue, 1.5 σ contour) of the 2F data set. **d,** *Polder mF$_o$-DF$_c$* map (green, 4 σ contour) of the 2F data set. **e,** *2mF$_o$-DF$_c$* map (blue, 1.5 σ contour) of the 2F-NH$_3$ data set. **f,** *Polder mF$_o$-DF$_c$* map (green, 4 σ contour) of the 2F-NH$_3$ data set. **g,** Standard *mF$_o$-DF$_c$* omit map (green, 3 σ contour) of the 2F-NH$_3$ data set after simulated annealing. **h,** *Polder mF$_o$-DF$_c$* map (green, 4 σ contour) of the 2F-NH$_3$ data set after simulated annealing.

Extended Data Figure 3. Dark RT vs Suga cryogenic vs Hellmich cryogenic

The present RT dark state structure is shown in grey, the Suga XFEL[7] in cyan and the Hellmich[16] cryogenic structure in purple. **a,** Overlay of the RT and Suga structures. **b,** Overlay of the RT and the Hellmich[16] structures. A large-scale rigid body motion of the two monomers with respect to each other and an in-plane expansion of each PS II monomer in the RT structure are visible. Comparison of TMH 2 of subunit CP47 between the dark state and the cryogenic XFEL structures[7] (**c**), the dark state and the Hellmich[16] cryogenic structures (**d**) and between the two cryogenic structures (**e**). The two cryogenic datasets reflect crystals with different packing. View is from the cytoplasmic side (top) or along the membrane plane (bottom). Despite the different packing only a small shift of 0.1-0.2 Å is observed between the two cryogenic structures. In contrast, the RT structure exhibits a larger shift of 0.5-0.6 Å in the positions of TMH 2 with respect to the cryogenic structures in both crystal forms, well above the error margin in our data. The cryogenic structures were superposed onto our dark structure model in PyMOL[71] using monomer 1 for alignment.
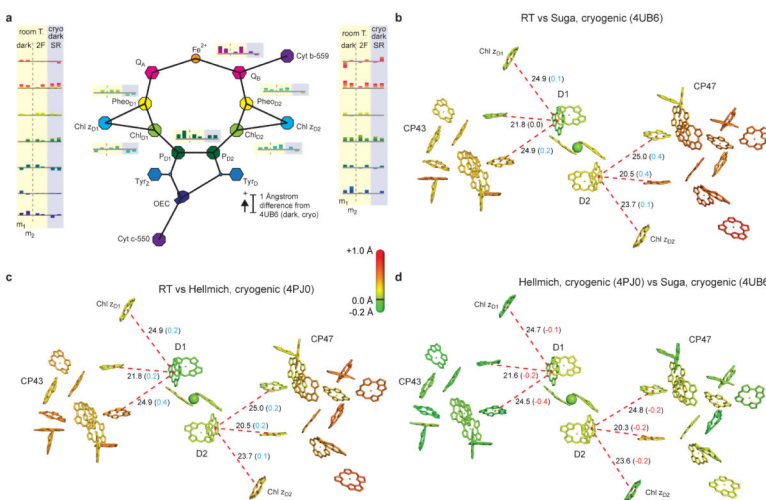
Extended Data Figure 4. Comparisons of the cofactor-cofactor distances in the crystal structures collected at cryogenic temperature and RT

a, Distances for central cofactors; the histogram shows the deviation of the cofactor-cofactor distances in the cryogenic SR dark state structure (Hellmich *et al.*, 4PJ0[16], highlighted in

blue) and in the dark and 2F RT structures (the present study, highlighted in yellow) from those of the cryogenic XFEL structure reported by Suga *et al.*[7] (4UB6). Changes are indicated by bars for monomers 1 and 2 (m_1, m_2), and color coding of bars matches the coloring of the associated pair of cofactors in the diagram. Among the differences, there is a consistent elongation in the distances involving Chl_Z as well as in the Q_B-Cyt b-559 and OEC-Cyt c-550 distances of both monomers in the RT data. In other cases, expansion of individual cofactor distances is observed in both RT structures and 4PJ0 relative to 4UB6 (*e.g.* P_{D2}-Chl_{D2}, Q_B-$Pheo_{D2}$), and in the case of P_{D1}-P_{D2} on average the elongation is more pronounced at RT compared to in the cryogenic structures. Changes in Chl positions between the RT dark structure vs. Suga *et al.* (4UB6) (**b**), between the RT dark structure and Hellmich *et al.* (4PJ0) that have the same dimer-dimer packing (**c**), and between Hellmich *et al.* (4PJ0) and Suga *et al.* (4UB6) (**d**). Distances of the Chl ring centers from the membrane normal passing through the center between $Pheo_{D1}$ and $Pheo_{D2}$ are computed and relative changes with respect to the values obtained from 4UB6 or 4PJ0 are shown as color coding on a rainbow scale from green (0.2 Å contraction) to red (1.0 Å expansion). For selected Chl-Chl pairs, distances are given with the absolute change in parentheses.
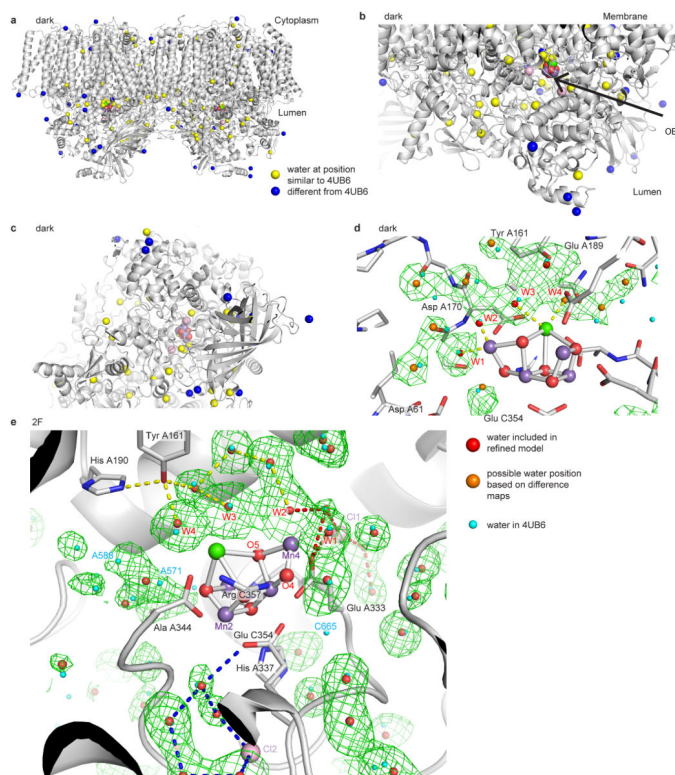
**Extended Data Figure 5. Location of water molecules observed in the RT structure**
a, Water positions refined in the dark RT structure of the PS II dimer are indicated by blue and yellow spheres. View is along the membrane plane with the cytoplasm on top and lumen on the bottom. Waters whose positions coincide with waters located in the cryogenic XFEL structure[7] (4UB6) are colored in yellow and waters in other positions are colored in dark blue. **b,** Enlarged view of the lumenal region showing the OEC of one monomer (magenta, red and green spheres for Mn, O and Ca) as well as the two Cl^- (pink spheres) located close

to the OEC. **c,** Waters located at the lumenal side of one monomer. View is from the lumenal side onto the membrane plane, with color coding as in **a** and **b**. **d,** *Polder* omit maps (2.5 σ contour, green mesh) for waters in the direct vicinity of the OEC in the dark state. Waters included in the refined model are indicated as red spheres, additional waters placed based on *polder* maps as orange spheres, and waters from 4UB6 are shown in light cyan. **e,** Possible water networks next to the OEC. Waters included in the refined model of the 2F state are indicated as red spheres and waters from 4UB6 are shown in light cyan. *Polder* omit maps (2.0 σ contour, green mesh, carved at 2 Å around water positions from 4UB6) confirm the positions of the refined waters and indicate the presence of additional waters (*e.g.* A571, A588), but no omit map density was observed at the position of water C665. The starting points of three water/proton channels postulated by Umena *et al.*[21] are indicated by dashed red, yellow, and blue lines.
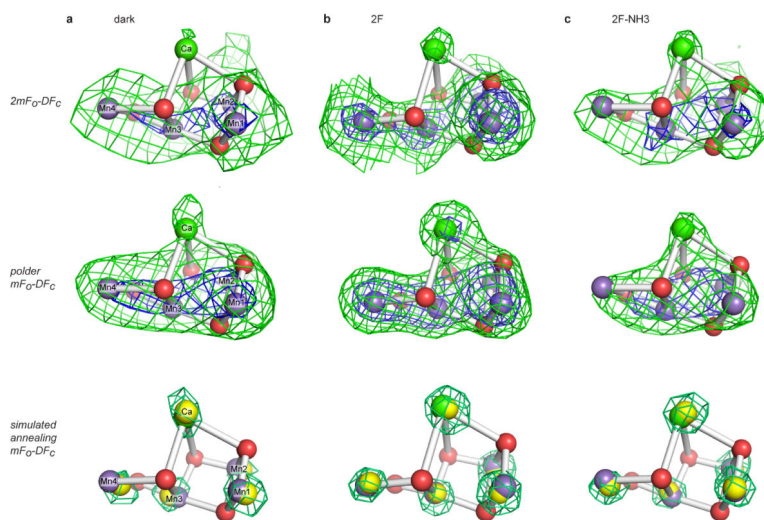
Extended Data Figure 6. Room temperature electron density of the Mn_4CaO_5 cluster
a, The *$2mF_O$-DF_c* electron density (top) contoured at 4.0 σ (green) and 8.0 σ (blue mesh) and the *polder mF_O-DF_c* electron density (middle) of the dark data set after omitting the OEC and real space refinement contoured at 8.0 σ (green) and 14.0 σ (blue mesh). At the bottom, the *mF_O-DF_c* electron density after omitting individual metal atoms and refining with simulated annealing is shown contoured at 4.0 σ (Ca), 7.0 σ (Mn1, Mn2), 8.0 σ (Mn3) and 4.0 σ (Mn4), respectively. The model of the OEC is shown with Mn as magenta, Ca as green and oxygen as red spheres overlaid with yellow spheres indicating the centers of the obtained omit densities. **b,** The *$2mF_O$-DF_c* electron density (top) contoured at 3.0 σ (green) and 6.0 σ (blue mesh) and the *polder mF_O-DF_c* electron density (middle) of the 2F data set after omitting the OEC and real space refinement contoured at 8 σ (green) and 14 σ (blue mesh). At the bottom, the *mF_O-DF_c* electron density after omitting individual metal atoms and refining with simulated annealing is shown contoured at 12.0 σ (Ca, Mn1, Mn3), 13.0 σ (Mn2) and 10.0 σ (Mn4), respectively, color coding as in a. **c,** The *$2mF_O$-DF_c* electron density (top) contoured at 5.0 σ (green) and 8.0 σ (blue mesh) and the *polder mF_O-DF_c* electron density (middle) of the 2F data set after omitting the OEC and real space refinement contoured at 11 σ (green) and 16 σ (blue mesh). At the bottom, the *mF_O-DF_c* electron density after omitting individual metal atoms and refining with simulated annealing is shown

contoured at 5.0 σ (Ca), 10.0 σ (Mn1), 8.0 σ (Mn2, Mn4) and 11.0 σ (Mn3), respectively, color coding as in a.
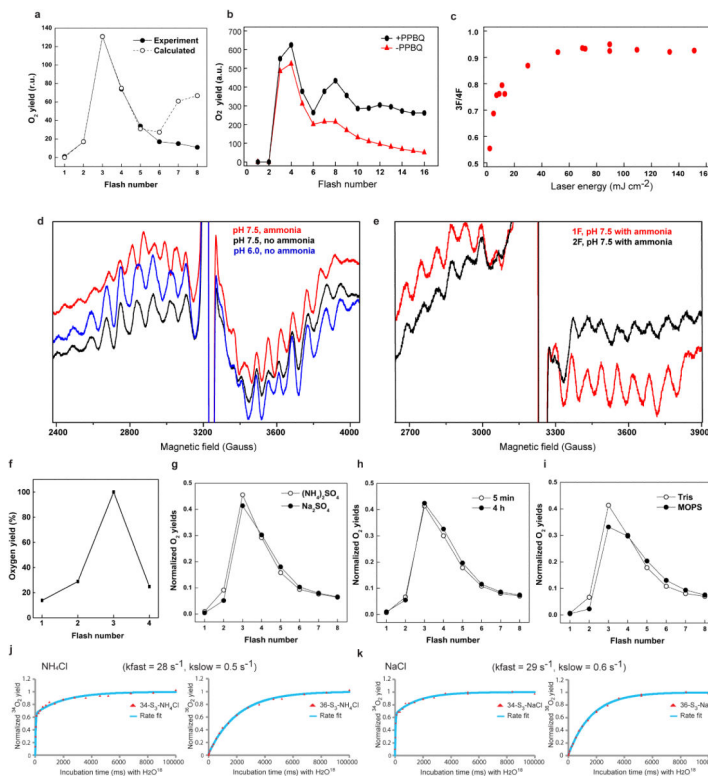
**Extended Data Figure 7. Characterization of PS II samples and substrate water exchange rates in the S$_3$ state**

a, Flash induced O$_2$ evolution pattern (FIOP) of a suspension of the native PS II core complexes (PSIIcc) at pH 6.5. Fit parameter: 100% S$_1$ in the dark, miss = 20%, double hit 4%, damping 2%, fit done on first 5 flashes. In the 2F sample, if double hits are excluded, ~60% of the S$_3$ population was calculated, with ~30% of S$_2$ and ~4% of S$_1$. **b,** Flash induced O$_2$ evolution pattern of a suspension of the PS IIcc (TRIS, pH 7.5, 100 mM (NH$_4$)$_2$SO$_4$) with and without PPBQ measured with 12 s between flashes using the thin layer MIMS setup (Methods) and 532 nm laser flash illumination: an increase in O$_2$ yield by 15% was observed if PPBQ was added. **c,** Light saturation in the thin layer MIMS set up resembling the illumination conditions of the DOT approach. The ratio of the oxygen yield of the third flash over that of the fourth flash is plotted as a qualitative measure for the miss parameter, which is minimal when the ratio is large. **d,** EPR spectra of native (pH 6.0 and 7.5) and ammonia-treated (pH 7.5) PS II solutions after continuous illumination at 195 K for one minute followed by annealing to 260 K for 30 seconds. Spectrometer condition: microwave frequency, 9.23 GHz; field modulation amplitude, 32 G at 100 KHz; microwave power, 20 mW. The spectra are collected at 7 K. **e,** EPR spectra of ammonia-treated (pH 7.5) PS II solution after applying one (red) or two (black) flashes. Spectrometer conditions are same as in A. **f,** O$_2$-flash pattern of PS II crystals at pH 7.5 (TRIS, (NH$_4$)$_2$SO$_4$) measured by MIMS with the replica set up for jet illumination described above. **g,** FIOP (Joliot-type electrode) of PSIIcc at pH 7.5 and 20°C in TRIS buffer with either 100 mM (NH$_4$)$_2$SO$_4$ or 100 mM

Na$_2$SO$_4$ addition. The O$_2$ yields for each sample were normalized to the O$_2$ yields induced by flashes 3-6 (Y3-6). No artificial electron acceptors were added. The flash frequency of the Xe-flash lamp was 2 Hz, and the Chl concentration of 0.4 mM. Data are the average of three technical replicates. From the data, a miss parameter of 23-25% and an S$_3$ state population of 50-53% can be extracted for both sample types. Double hits, caused by the Xe flash lamp, are 3-6%, and are absent under laser flash illumination used during the XFEL experiments. The total O$_2$ yield of the ammonia-containing sample was 66% of the Na$_2$SO$_4$ control, and 52% of the FIOP at pH 6.5 (panel a). **h,** Flash induced O$_2$ evolution pattern of PS II core sample incubated in TRIS and 100 mM (NH$_4$)$_2$SO$_4$ for 5 min at pH 7.6 versus one that was incubated for 4 h at RT. No degradation of the sample was observed over time (O$_2$ yields of both FOIPs normalized to Y3-6 of 4 min trace). **i,** Flash induced O$_2$ evolution pattern of PS II core sample containing TRIS and 100 mM (NH$_4$)$_2$SO$_4$ versus one containing MOPS and 100 mM (NH$_4$)$_2$SO$_4$. Both FIOPs normalized to Y3-6 of TRIS containing sample. Substrate water exchange was measured for the S$_3$ state of PS II core complexes at pH 7.6/20°C as described in 2,4,12 in a Hepes buffer containing 100 mM NH$_4$Cl (**j**) or 100 mM NaCl (**k**). The left panels show the biphasic rise of the mass 34 peak (^{16}O^{18}O), while the right side shows the simultaneously recorded monophasic rise of the 36 peak of the double exchanged ^{18}O^{18}O. Red symbols represent the individually measured data points, while the blue lines are the kinetic simulations. Nearly identical rates for the exchange of the fast (k$_{fast}$) and slow (k$_{slow}$) substrates were found with and without ammonia.
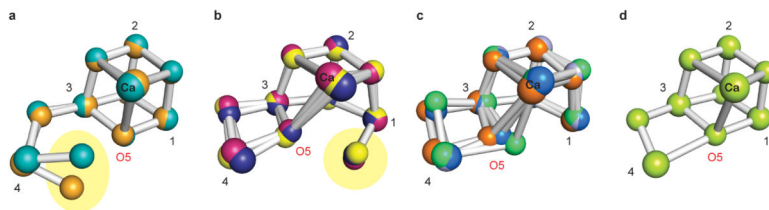
Extended Data Figure 8. Possible Mn$_4$CaO$_5$ complex models for the S$_3$-state proposed in the literature

The models are grouped into four classes (**a, b, c, d,** see below). Mn are numbered (1 to 4) in the same manner as in the main paper. **a,** Models with an inserted water (highlighted in yellow) on the left side (closed cubane proposed as a transient S$_3$-state by Cox *et al.*[64] in teal; Isobe *et al.* 3cL[65] in light orange) shift Mn4 the furthest out. **b,** Models with an inserted water (highlighted in yellow) on the right side (model by Cox *et al.*[64] in yellow; Li *et al.*[66] in pink; Ichino *et al.* model 3[67] in dark blue) closely resemble models with an open cubane, and were proposed initially by Siegbahn[23]. **c,** Other models with no inserted water: Ichino model 1[67] in marine blue; Suga (4UB6)[7] in green; Ichino model 2[67] in lavender; Isobe *et al.*[65] model 3aR in dark orange). **d,** Only one proposed model featured a closed cubane with no inserted water (Hatakeyama *et al.*[68] in yellow-green). Note that, except for the type **a** structure (a complete cubane plus mono-μ-oxo bridged Mn4) and the type **d** structure (a closed cubane with no water inserted), the Mn atomic positions are very similar in all models within 0.26 Å. Even the Mn4 positions between the type **a** and other models differ only by 0.73 Å. On the other hand, the O5 position is expected to differ among the models by at most 1.52 Å.
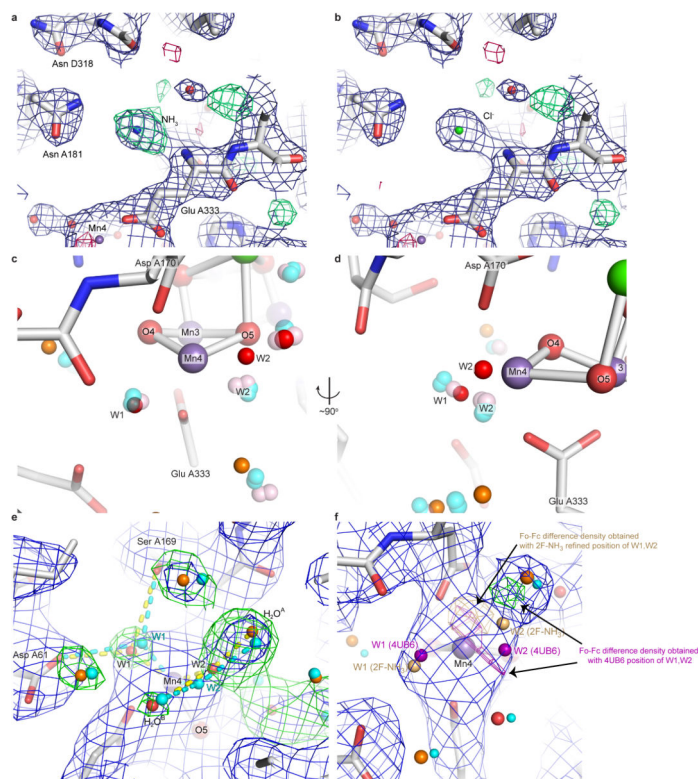
Extended Data Figure 9. The electron density of the Cl⁻ binding sites and environment of the W1 and W2 sites at the OEC in the 2F-NH₃ samples in the 2F dataset

a, The Cl⁻ binding site 1 with Cl⁻ (green sphere) at its refined position. The *2mF$_O$-DF$_c$* map (blue mesh) is shown at 1.5 σ, and the *mF$_O$-DF$_c$* map (green/red) is shown at +/− 3 σ. **b,** The Cl⁻ binding site 1 with ammonia (blue sphere) instead of Cl⁻ included in the model. Lack of difference density at the Cl⁻ position in the refined model and the positive difference density observed when ammonia is substituted for Cl⁻ indicate that ammonia does not account for the electron density and that Cl⁻ is a good model for the observed density. **c, d,** Comparison of the positions of W1 and W2 between the 2F-NH₃ (red), 2F (light pink) and cryogenic S₁ XFEL[7] (light cyan) structures in two different orientations. The outcome of two different alignment procedures (to optimize overlap of either OEC Mn atoms or the surrounding protein ligands) are shown illustrating the error in these alignments. A small shift of both W1 and W2 upon transition from the cryogenic S₁ XFEL to the 2F structure is visible. In the 2F-NH₃ model, W1 is shifted slightly further along the same direction as the dark-2F difference. In contrast, the displacement of W2 in the 2F-NH3 model is significantly larger than that between the S₁ XFEL and 2F structure. **e,** *2mF$_O$-DF$_c$* electron density (blue, 1.0 σ) of the 2F-NH₃ data set around Mn4, and *polder* omit maps at 3.5 σ (green). Red spheres: Water refined in the current model; orange spheres: Water placed in the polder maps but not included in the refined model; cyan spheres: Water positions from the cryogenic XFEL structure. **f,** When calculating the *mF$_O$-DF$_c$* electron density using the refined positions of W1 and W2 (light orange spheres) from the 2F-NH₃ data, only a negative peak is observed (orange mesh, −3 σ contour) while using W1 and W2 positions (purple spheres) from the S₁ XFEL structure yields clear positive and negative peaks (green and purple mesh, ±3 σ contour, coloring of other waters as in **e**). This indicates that the W2 position from the S₁

XFEL structure does not provide a good fit to the observed electron density. However, at the present resolution the observed difference densities may be influenced by other effects, *e.g.* Fourier series truncations and the strong density of H_2O^A close to W2.

Extended Data Table 1

Data collection and refinement statistics for the RT dark (S1), 2F and 2F-NH_3 data

	S_1 dataset (5KAF)	2F dataset (5TIS)	2F-NH_3 dataset (5KAI)
Data collection			
Space group	$P2_12_12_1$	$P2_12_12_1$	$P2_12_12_1$
Cell dimensions			
a, b, c (Å)	117.7, 223.8, 330.8	117.9, 223.1, 310.7[a]	117.9, 224.3, 331.0
α, β, γ (°)	90, 90, 90	90, 90, 90	90, 90, 90
Wavelength (Å)	1.7493	1.3010	1.7492
Resolution (Å)	43.13-3.00 (3.05-3.00)[b]	44.28-2.25 (2.29-2.25)	43.58-2.80 (2.85-2.80)
Unique reflections	170444 (7698)	385065 (19084)	213400 (10235)
Completeness (%)	97.30 (88.80)	99.98 (99.98)	99.00 (95.96)
Multiplicity	8.48 (2.91)	158.47 (10.36)	13.70 (4.17)
$I/\sigma(I)$	10.51 (2.26)	19.83 (2.04)	11.62 (1.94)
$CC_{1/2}$	53.2 (13.2)	97.4 (1.8)	54.2 (7.3)
Wilson B-factor	61.05	42.98	60.41
Collection instrument	LCLS endstation CXI	LCLS endstations XPP and MFX	LCLS endstation CXI
Refinement			
R_{work} (%)	26.37 (33.50)	19.49 (34.04)	24.97 (33.98)
R_{free} (%)	30.30 (37.98)	23.08 (38.09)	29.97 (33.98)
No. atoms	50162	51757	50284
Protein residues	5319	5319	5316
Ligands	174	189	180
Waters	124	1179	107
Average B factor	47.3	45.9	56.6
R.m.s. deviations			
Bond lengths (Å)	0.004	0.005	0.004
Bond angles (°)	0.479	0.502	0.592
Ramachandran favored (%)	96.18	97.20	95.20
Ramachandran outliers (%)	0.19	0.29	0.57
MolProbity clashscore[69]	4.45	4.45	6.55

[a] Unit cell parameters were constrained for this data set.

[b] Values in parentheses are for the highest-resolution shell.

Supplementary Material

Refer to Web version on PubMed Central for supplementary material.

Authors

Iris D. Young[#1], Mohamed Ibrahim[#2], Ruchira Chatterjee[#1], Sheraz Gul[1], Franklin Fuller[1], Sergey Koroidov[3], Aaron S. Brewster[1], Rosalie Tran[1], Roberto Alonso-Mori[4], Thomas Kroll[5,6], Tara Michels-Clark[1], Hartawan Laksmono[5], Raymond G. Sierra[4,5], Claudiu A. Stan[5], Rana Hussein[2], Miao Zhang[2], Lacey Douthit[1], Markus Kubin[7], Casper de Lichtenberg[3], Pham Long Vo[3], Håkan Nilsson[3], Mun Hon Cheah[3], Dmitriy Shevela[3], Claudio Saracini[1], Mackenzie A. Bean[1], Ina Seuffert[2], Dimosthenis Sokaras[6], Tsu-Chien Weng[6,a], Ernest Pastor[1], Clemens Weninger[5], Thomas Fransson[5], Louise Lassalle[1], Philipp Bräuer[8,9], Pierre Aller[9], Peter T. Docker[9], Babak Andi[10], Allen M. Orville[9], James M. Glownia[4], Silke Nelson[4], Marcin Sikorski[4], Diling Zhu[4], Mark S. Hunter[4], Thomas J. Lane[4], Andy Aquila[4], Jason E. Koglin[4], Joseph Robinson[4], Mengning Liang[4], Sébastien Boutet[4], Artem Y. Lyubimov[11], Monarin Uervirojnangkoorn[11], Nigel W. Moriarty[1], Dorothee Liebschner[1], Pavel V. Afonine[1], David G. Waterman[12], Gwyndaf Evans[9], Philippe Wernet[7], Holger Dobbek[2], William I. Weis[11,13,14], Axel T. Brunger[11,13], Petrus H. Zwart[1], Paul D. Adams[1,15], Athina Zouni[2,*], Johannes Messinger[3,16,*], Uwe Bergmann[5], Nicholas K. Sauter[1], Jan Kern[1,4], Vittal K. Yachandra[1,*], and Junko Yano[1,*]

Affiliations

[1]Molecular Biophysics and Integrated Bioimaging Division, Lawrence Berkeley National Laboratory, Berkeley, CA 94720, USA.

[2]Institut für Biologie, Humboldt-Universität zu Berlin, D-10099 Berlin, Germany.

[3]Institutionen för Kemi, Kemiskt Biologiskt Centrum, Umeå Universitet, SE 90187 Umeå, Sweden.

[4]LCLS, SLAC National Accelerator Laboratory, Menlo Park, CA 94025, USA.

[5]Stanford PULSE Institute, SLAC National Accelerator Laboratory, Menlo Park, CA 94025, USA.

[6]SSRL, SLAC National Accelerator Laboratory, Menlo Park, CA 94025, USA.

[7]Institute for Methods and Instrumentation on Synchrotron Radiation Research, Helmholtz Zentrum, 14109 Berlin, Germany.

[8]Department of Biochemistry, University of Oxford, South Parks Road, Oxford OX1 3QU, UK.

[9]Diamond Light Source Ltd, Harwell Science and Innovation Campus, Didcot, Oxfordshire OX11 0DE, UK.

[10]National Synchrotron Light Source II, Brookhaven National Laboratory, Upton, NY, 11973, USA.

[11]Department of Molecular and Cellular Physiology, Stanford University, Stanford, CA 94305, USA.

[12]STFC Rutherford Appleton Laboratory, Didcot, OX11 0QX, UK and CCP4, Research Complex at Harwell, Rutherford Appleton Laboratory, Didcot, OX11 0FA, UK.

[13]Department of Photon Science, Stanford University, Stanford, CA 94305.

[14]Department of Structural Biology, Stanford University, Stanford, CA 94305.

[15]Department of Bioengineering, University of California Berkeley, Berkeley, CA 94720.

[16]Department of Chemistry, Molecular Biomimetics, Ångström Laboratory, Uppsala University, SE 75237 Uppsala, Sweden.

Acknowledgments

References

1. Kok B, Forbush B, McGloin M. Cooperation of charges in photosynthetic O_2 evolution. 1. A linear 4-step mechanism. Photochem. Photobiol. 1970; 11:457–475. [PubMed: 5456273]

2. Cox N, Messinger J. Reflections on substrate water and dioxygen formation. Biochim. Biophys. Acta. 2013; 1827:1020–1030. [PubMed: 23380392]

3. Yano J, Yachandra V. Mn_4Ca cluster in photosynthesis: Where and how water is oxidized to dioxygen. Chem. Rev. 2014; 114:4175–4205. [PubMed: 24684576]

4. Messinger J, Badger M, Wydrzynski T. Detection of one slowly exchanging substrate water molecule in the S_3 state of photosystem II. Proc. Natl. Acad. Sci. U. S. A. 1995; 92:3209–3213. [PubMed: 11607525]

5. Hillier W, Wydrzynski T. ^{18}O-Water exchange in photosystem II: Substrate binding and intermediates of the water splitting cycle. Coord. Chem. Rev. 2008; 252:306–317.

6. Ugur I, Rutherford AW, Kaila VR. Redox-coupled substrate water reorganization in the active site of Photosystem II-The role of calcium in substrate water delivery. Biochim. Biophys. Acta. 2016; 1857:740–748. [PubMed: 26826591]

7. Suga M, et al. Native structure of photosystem II at 1.95 Å resolution viewed by femtosecond X-ray pulses. Nature. 2015; 517:99–103. [PubMed: 25470056]

8. Fraser JS, et al. Accessing protein conformational ensembles using room-temperature X-ray crystallography. Proc. Natl. Acad. Sci. U. S. A. 2011; 108:16247–16252. [PubMed: 21918110]

9. Tilton RF, Dewan JC, Petsko GA. Effects of temperature on protein-structure and dynamics - X-ray crystallographic studies of the protein ribonuclease a at 9 different temperatures from 98K to 320K. Biochemistry. 1992; 31:2469–2481. [PubMed: 1547232]

10. Boussac A, Rutherford AW, Styring S. Interaction of ammonia with the water splitting enzyme of photosystem II. Biochemistry. 1990; 29:24–32. [PubMed: 2157480]

11. Britt RD, Zimmermann JL, Sauer K, Klein MP. The state of manganese in the photosynthetic apparatus. 10. Ammonia binds to the catalytic Mn of the oxygen-evolving complex of photosystem-II - evidence by electron-spin echo envelope modulation spectroscopy. J. Am. Chem. Soc. 1989; 111:3522–3532.

12. Navarro MP, et al. Ammonia binding to the oxygen-evolving complex of photosystem II identifies the solvent-exchangeable oxygen bridge (μ-oxo) of the manganese tetramer. Proc. Natl. Acad. Sci. U. S. A. 2013; 110:15561–15566. [PubMed: 24023065]

13. Oyala PH, Stich TA, Debus RJ, Britt RD. Ammonia binds to the dangler manganese of the photosystem II oxygen-evolving complex. J. Am. Chem. Soc. 2015; 137:8829–8837. [PubMed: 26083545]

14. Kupitz C, et al. Serial time-resolved crystallography of photosystem II using a femtosecond X-ray laser. Nature. 2014; 513:261–265. [PubMed: 25043005]

15. Sauter NK, et al. No observable conformational changes in PSII. Nature. 2016; 533:E1–E2. [PubMed: 27193689]

16. Hellmich J, et al. Native-like photosystem II superstructure at 2.44 Å resolution through detergent extraction from the protein crystal. Structure. 2014; 22:1607–1615. [PubMed: 25438669]

17. Moser CC, Keske JM, Warncke K, Farid RS, Dutton PL. Nature of biological electron transfer. Nature. 1992; 355:796–802. [PubMed: 1311417]

18. Förster T. Zwischenmolekulare Energiewanderung und Fluoreszenz. Ann. Phys. 1948; 437:55–75.

19. Umena Y, Kawakami K, Shen J-R, Kamiya N. Crystal structure of oxygen- evolving photosystem II at a resolution of 1.9 Å. Nature. 2011; 473:55–60. [PubMed: 21499260]

20. Cox N, et al. Electronic structure of the oxygenevolving complex in photosystem II prior to O-O bond formation. Science. 2014; 345:804–808. [PubMed: 25124437]

21. Siegbahn PEM. Structures and energetics for O_2 formation in photosystem II. Acc. Chem. Res. 2009; 42:1871–1880. [PubMed: 19856959]

22. Glöckner C, et al. Structural changes of the oxygen-evolving complex in photosystem II during the catalytic cycle. J. Biol. Chem. 2013; 288:22607–22620. [PubMed: 23766513]

23. Li XC, Siegbahn PEM. Alternative mechanisms for O-2 release and O-O bond formation in the oxygen evolving complex of photosystem II. Phys. Chem. Chem. Phys. 2015; 17:12168–12174. [PubMed: 25879997]

24. Kern J, et al. Taking snapshots of photosynthetic water oxidation using femtosecond X- ray diffraction and spectroscopy. Nat. Commun. 2014; 5:4371. [PubMed: 25006873]

25. Beck WF, Depaula JC, Brudvig GW. Ammonia binds to the manganese site of the O_2-evolving complex of photosystem II in the S_2 state. J. Am. Chem. Soc. 1986; 108:4018–4022.

26. Hou LH, Wu CM, Huang HH, Chu HA. Effects of ammonia on the structure of the oxygen-evolving complex in photosystem II as revealed by light-induced FTIR difference spectroscopy. Biochemistry. 2011; 50:9248–9254. [PubMed: 21942297]

27. Askerka M, Vinyard DJ, Brudvig GW, Batista VS. NH_3 binding to the S_2 state of the O_2-evolving complex of photosystem II: Analogue to H_2O binding during the $S_2 \to S_3$ transition. Biochemistry. 2015; 54:5783–5786. [PubMed: 26378340]

28. Retegan M, et al. A five-coordinate Mn(IV) intermediate in biological water oxidation: spectroscopic signature and a pivot mechanism for water binding. Chem. Sci. 2016; 7:72–84.

29. Pecoraro VL, Baldwin MJ, Caudle MT, Hsieh WY, Law NA. A proposal for water oxidation in photosystem II. Pure Appl. Chem. 1998; 70:925–929.

30. Vrettos JS, Limburg J, Brudvig GW. Mechanism of photosynthetic water oxidation: combining biophysical studies of photosystem II with inorganic model chemistry. Biochim. Biophys. Acta. 2001; 1503:229–245. [PubMed: 11115636]

31. Yamanaka S, et al. Possible mechanisms for the O-O bond formation in oxygen evolution reaction at the $CaMn_4O_5(H_2O)(4)$ cluster of PSII refined to 1.9 angstrom X-ray resolution. Chem.Phys. Letters. 2011; 511:138–145.

32. Kern J, et al. Purification, characterisation and crystallisation of photosystem II from Thermosynechococcus elongatus cultivated in a new type of photobioreactor. Biochim. Biophys. Acta. 2005; 1706:147–157. [PubMed: 15620375]

33. Ibrahim M, et al. Improvements in serial femtosecond crystallography of photosystem II by optimizing crystal uniformity using microseeding procedures. Struct. Dynam. 2015; 2:041705.

34. Long Vo P, Messinger J. Electrochemically produced hydrogen peroxide affects Joliot-type oxygen-evolution measurements of photosystem II. Biochim. Biophys. Acta. 2014; 1837:1411–1416. [PubMed: 24486444]

35. Beck WF, Brudvig GW. Binding of amines to the O_2-evolving center of photosystem II. Biochemistry. 1986; 25:6479–6486. [PubMed: 3024709]

36. Geijer P, Deak Z, Styring S. Proton equilibria in the manganese cluster of photosystem II control the intensities of the S_0 and S_2 state g ~2 electron paramagnetic resonance signals. Biochemistry. 2000; 39:6763–6772. [PubMed: 10841755]

37. Yano, J., et al. in Sustaining Life on Planet Earth: Metalloenzymes Mastering Dioxygen and Other Chewy Gases. Sosa, ME.; Torres, PMH.; Kroneck, editors. Vol. 15. Springer; 2015. p. 13-43.

38. Beckmann K, Messinger J, Badger MR, Wydrzynski T, Hillier W. On-line mass spectrometry: membrane inlet sampling. Photosynth. Res. 2009; 102:511–522. [PubMed: 19653116]

39. Sierra RG, et al. Nanoflow electrospinning serial femtosecond crystallography. Acta Cryst. D. 2012; 68:1584–1587. [PubMed: 23090408]

40. Sierra RG, et al. Concentric-flow electrokinetic injector enables serial crystallography of ribosome and photosystem II. Nat. Methods. 2016; 13:59–62. [PubMed: 26619013]

41. Chollet M, et al. The X-ray Pump-Probe instrument at the Linac Coherent Light Source. J. Synchrotron Rad. 2015; 22:503–507.

42. Boutet S, Williams GJ. The Coherent X-ray Imaging (CXI) instrument at the Linac Coherent Light Source (LCLS). New J. Phys. 2010; 12:035024.

43. Fuller FD, et al. Drop-on-Demand Sample Delivery for Studying Biocatalysts in Action at XFELs submitted. 2016

44. Liang M, et al. The Coherent X-ray Imaging instrument at the Linac Coherent Light Source. J. Synchrotron Radiat. 2015; 22:514–519. [PubMed: 25931062]

45. Sauter NK, Hattne J, Grosse-Kunstleve RW, Echols N. New Python-based methods for data processing. Acta Crystallogr. D. 2013; 69:1274–1282. [PubMed: 23793153]

46. Hattne J, et al. Accurate macromolecular structures using minimal measurements from X-ray free-electron lasers. Nat. Methods. 2014; 11:545–548. [PubMed: 24633409]

47. Herrmann S, et al. CSPAD upgrades and CSPAD V1.5 at LCLS. J. Physics. 2014; 493:012013.

48. Steller I, Bolotovsky R, Rossmann MG. An algorithm for automatic indexing of oscillation images using Fourier analysis. J. Appl. Crystallogr. 1997; 30:1036–1040.

49. Rossmann MG, van Beek CG. Data processing. Acta Crystallogr. D. 1999; 55:1631–1640. [PubMed: 10531511]

50. Sauter NK, Grosse-Kunstleve RW, Adams PD. Robust indexing for automatic data collection. J. Appl. Crystallogr. 2004; 37:399–409. [PubMed: 20090869]

51. Sauter NK, et al. Improved crystal orientation and physical properties from single-shot XFEL stills. Acta Crystallogr. D. 2014; 70:3299–3309. [PubMed: 25478847]

52. Sauter NK, Grosse-Kunstleve RW, Adams PD. Improved statistics for determining the Patterson symmetry from unmerged diffraction intensities. J. Appl. Crystallogr. 2006; 39:158–168.

53. Waterman DG, et al. Diffraction-geometry refinement in the DIALS framework. Acta Crystallogr. D. 2016; 72:558–575.

54. Sauter NK. XFEL diffraction: developing processing methods to optimize data quality. J. Synchrotron Radiat. 2015; 22:239–248. [PubMed: 25723925]

55. Zhang Z, Sauter NK, van den Bedem H, Snell G, Deacon AM. Automated diffraction image analysis and spot searching for high-throughput crystal screening. J. Appl. Cryst. 2006; 39:112–119.

56. Uervirojnangkoorn M, et al. Enabling X-ray free electron laser crystallography for challenging biological systems from a limited number of crystals. Elife. 2015; 4:e05421.

57. McCoy AJ, et al. Phaser crystallographic software. J. Appl. Crystallogr. 2007; 40:658–674. [PubMed: 19461840]

58. Afonine PV, et al. Towards automated crystallographic structure refinement with phenix.refine. Acta Crystallogr. D. 2012; 68:352–367. [PubMed: 22505256]

59. Padilla JE, Yeates TO. A statistic for local intensity differences: robustness to anisotropy and pseudo-centering and utility for detecting twinning. Acta Crystallogr. D. 2003; 59:1124–1130. [PubMed: 12832754]

60. Adams PD, et al. PHENIX: a comprehensive Python-based system for macromolecular structure solution. Acta Crystallogr. D. 2010; 66:213–221. [PubMed: 20124702]

61. Emsley P, Lohkamp B, Scott WG, Cowtan K. Features and development of Coot. Acta Crystallogr. D. 2010; 66:486–501. [PubMed: 20383002]

62. Schrödinger LLC. The PyMOL molecular graphics system, version 1.8. 2015

63. Liebschner D, et al. Polder maps: Improving OMIT maps by excluding bulk-solvent. Acta Crystallogr. D. 2016 in press.

64. Cox N, Pantazis DA, Neese F, Lubitz W. Biological water oxidation. Acc. Chem. Res. 2013; 46:1588–1596. [PubMed: 23506074]

65. Isobe H, et al. Theoretical illumination of water-inserted structures of the $CaMn_4O_5$ cluster in the S_2 and S_3 states of oxygen-evolving complex of photosystem II: full geometry optimizations by B3LYP hybrid density functional. Dalton Trans. 2012; 41:13727–13740. [PubMed: 23037319]

66. Li X, Siegbahn PEM, Ryde U. Simulation of the isotropic EXAFS spectra for the S_2 and S_3 structures of the oxygen evolving complex in photosystem II. Proc. Natl. Acad. Sci. U. S. A. 2015; 112:3979–3984. [PubMed: 25775575]

67. Ichino T, Yoshioka Y. Theoretical study on mechanism of dioxygen evolution in photosystem II. II. Molecular and electronic structures at the S_3 and S_4 states of oxygen-evolving complex. Chem. Phys. Letts. 2014; 595:237–241.

68. Hatakeyama M, et al. Structural changes in the S_3 state of the oxygen evolving complex in photosystem II. Chem. Phys. Letts. 2016; 651:243–250.

69. Chen VB, et al. MolProbity: all-atom structure validation for macromolecular crystallography. Acta Crystallogr. D. 2010; 66:12–21. [PubMed: 20057044]
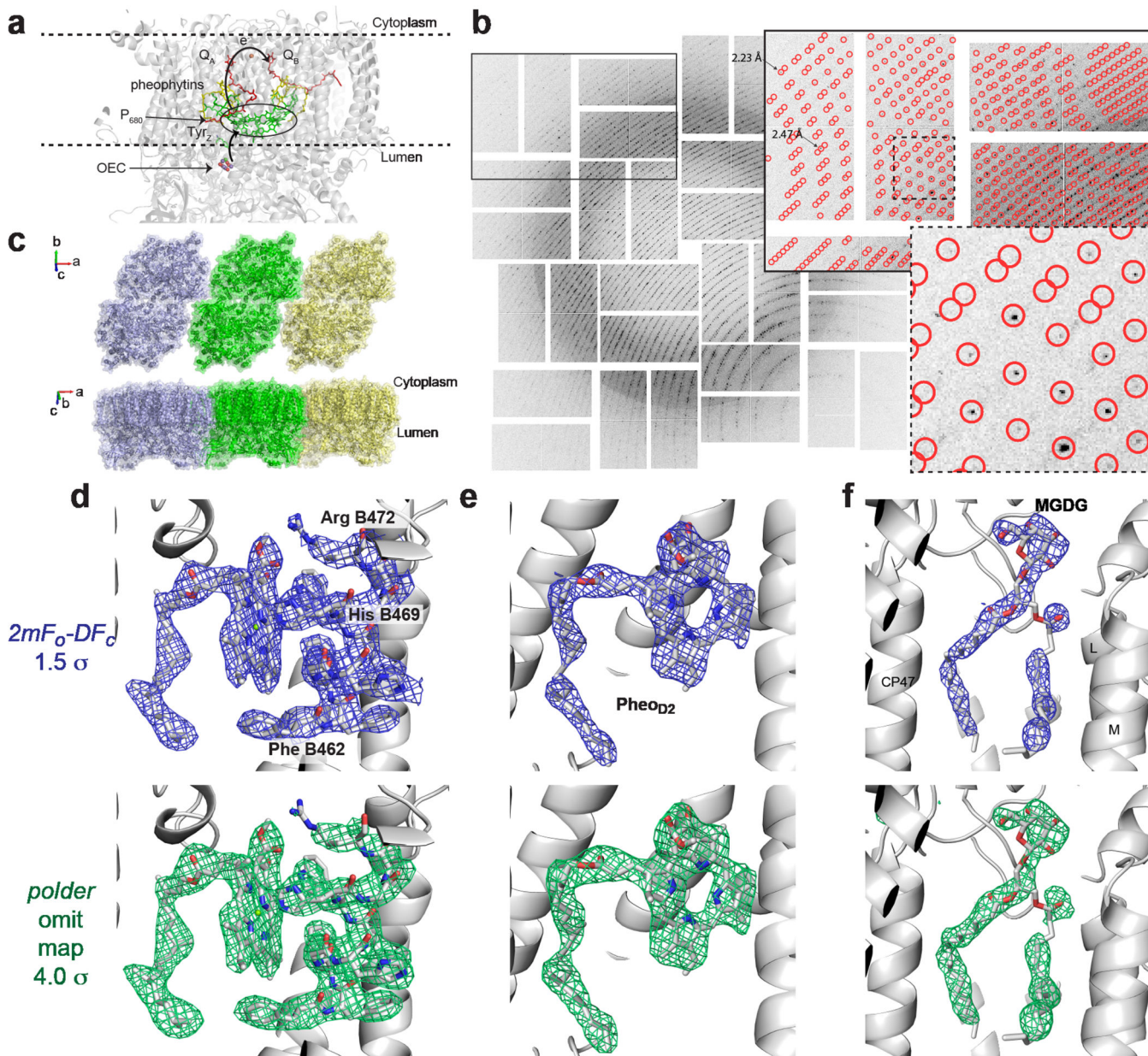
Figure 1. Crystal structure of PS II in the dark (S$_1$) state collected at RT with fs XFEL pulses
a, Schematic overview of the reaction center of PS II showing cofactors involved in light induced electron transfer and water oxidation. **b,** Diffraction pattern of a PS II microcrystal. The insets show enlarged views with the indexing solution. **c,** Arrangement of dimers in the unit cell of the crystals. Three dimers (blue, green, yellow) with the view onto the membrane plane from the lumenal side (top) and with the view along the membrane plane (bottom). (**d - f**) Examples of omit maps with the model (grey). **d,** TMH 6 of CP47 with a Chl; **e,** Pheophytin in subunit D2; **f,** Monogalactosyl diacylglycerol (MGDG) lipid next to CP47.
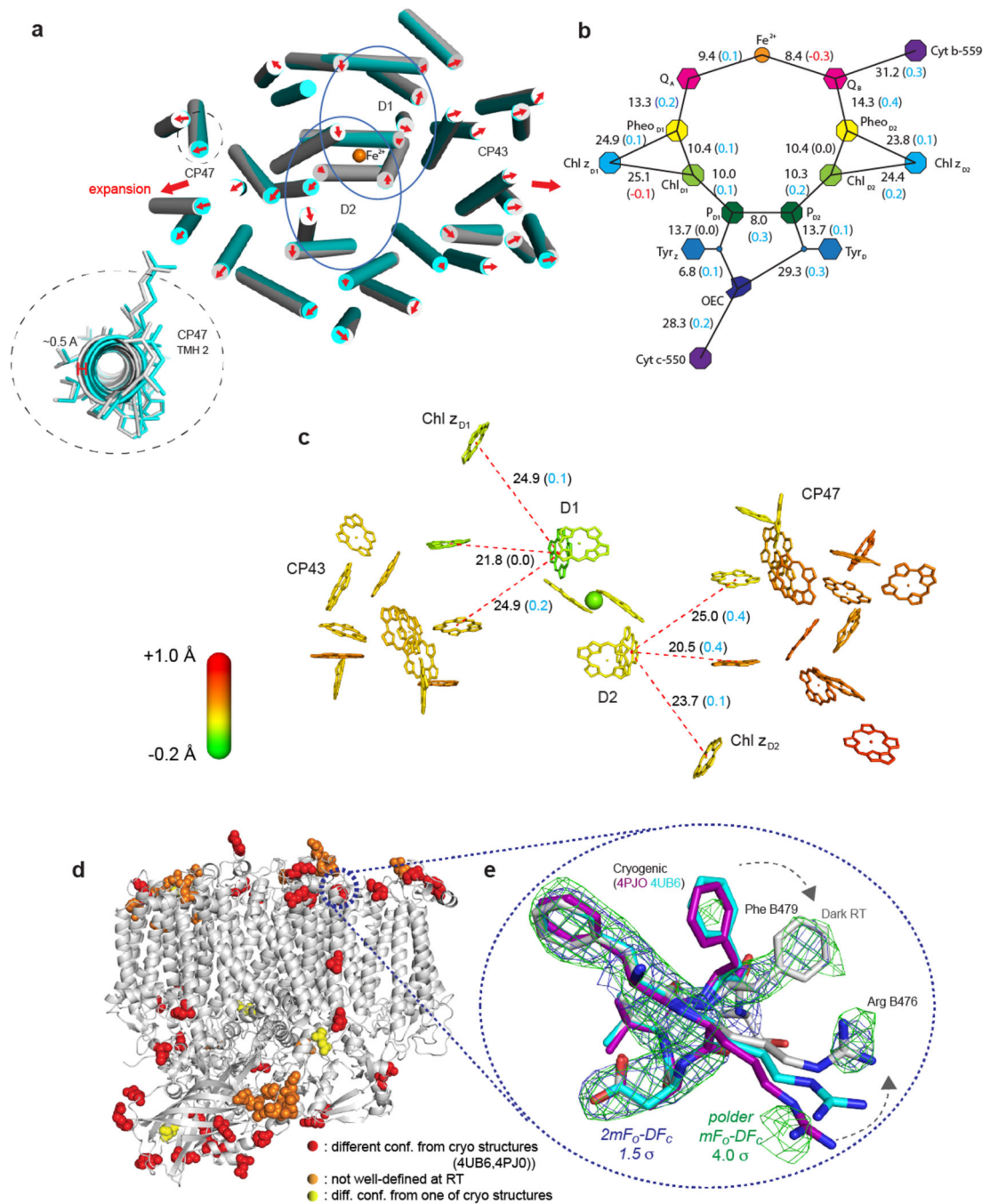
Figure 2. Comparison of the RT and cryogenic structures in the dark state

a, Location of TMHs in one monomer at RT (grey cylinders) and the cryogenic structure[7] (cyan). View is onto the membrane plane from the cytoplasmic side. One TMH is shown enlarged in the inset to illustrate the shift between the cryogenic and RT structures. **b,** Distances between the cofactors of the electron transport chain in the dark structure, with differences to the cryogenic structure[7] in parentheses. **c,** Changes in Chl/Pheo distances, represented by color. **d,** Location of residues that show different side chain orientations at RT compared to the cryogenic structures[7,16]. **e,** Examples of different side chain positions in

the RT structure (grey) with the cryogenic structures (cyan[7], purple[16]). Dashed lines indicate the location of these residues in the PS II complex.
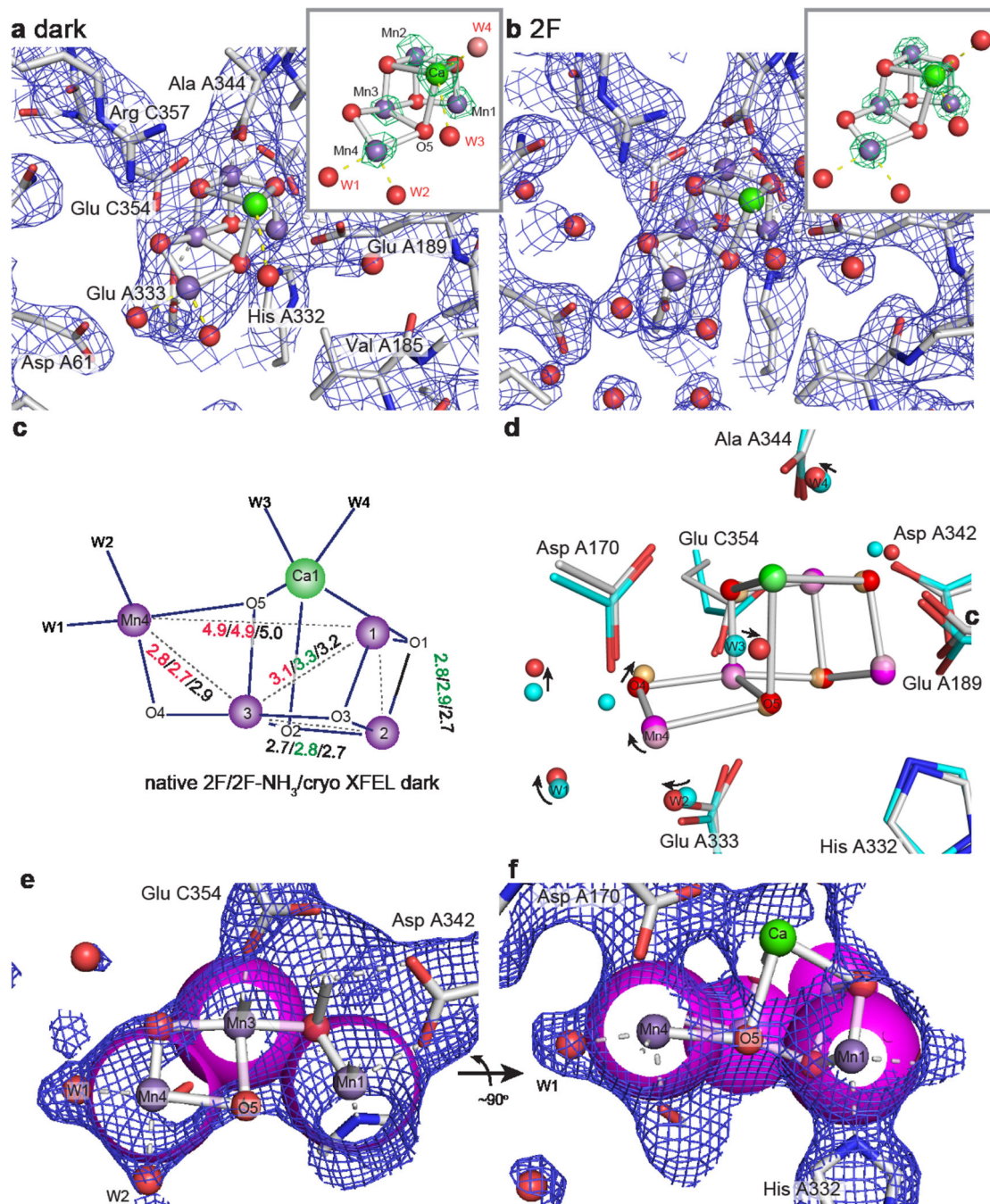
Figure 3. The oxygen evolving complex
Electron density around the OEC of the dark (**a**) and 2F (**b**) RT structures; insets: individual metal atom omit maps. **c,** Mn-Mn distances obtained from metal omit maps for the 2F and 2F-NH$_3$ data compared with the distances from ref[7]. **d,** Perturbations in the vicinity of the Mn$_4$CaO$_5$ cluster in the 2F state (grey) in comparison to ref[7] (cyan). **e, f,** Electron density in the Mn1-O5-Mn4 region in two different orientations. Density (blue mesh, half the grid spacing compared to other maps shown) is contoured at 1.8 σ, matching the van der Waals radius (light magenta spheres) of Mn. Clear density protruding beyond the van der Waals

volume of the Mn is visible for metal bound waters (*e.g.* W1, W2) but no extra density is seen around Mn1, a proposed location of an inserted water in the Mn_4CaO_5 cluster in the S_3 state.
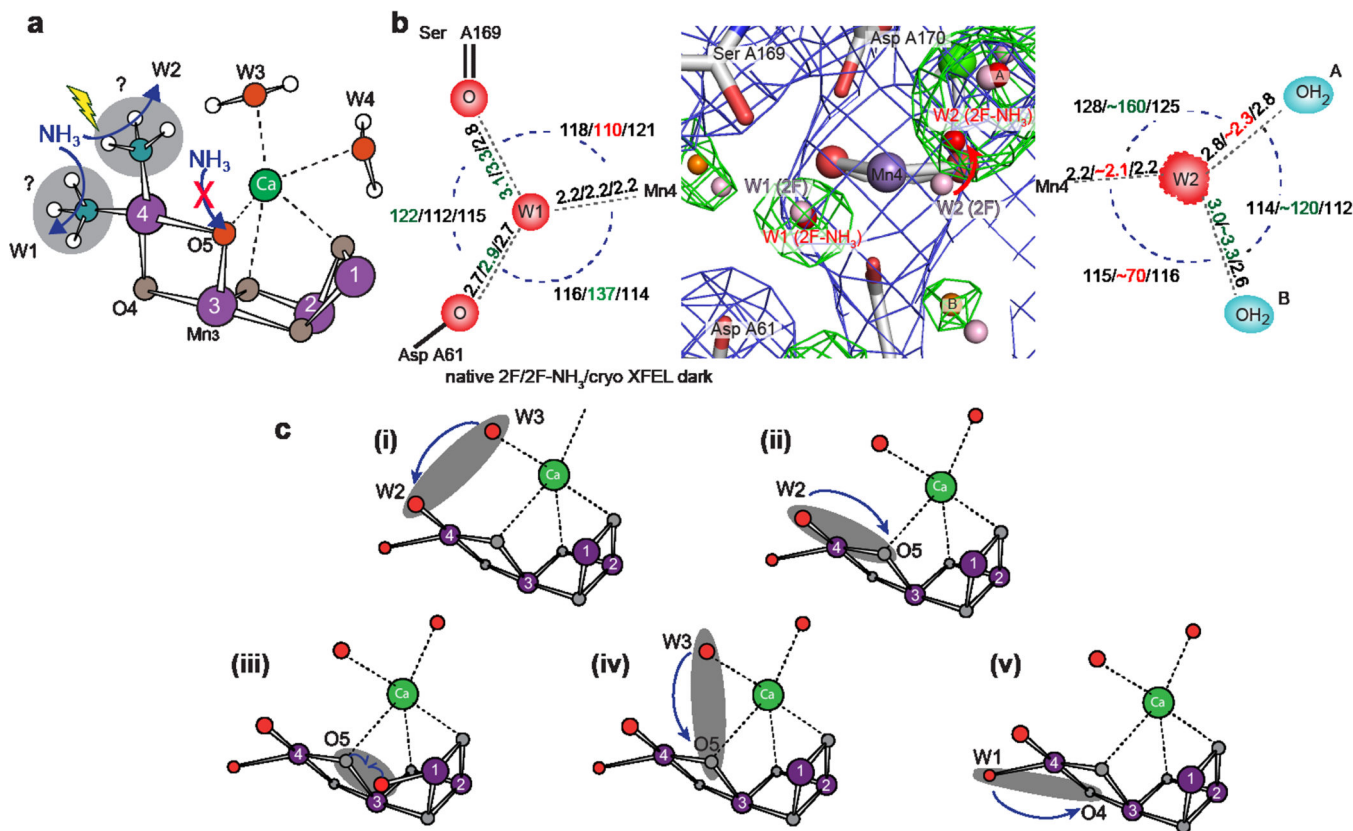
Figure 4. Ammonia binding sites to the OEC and O-O bond formation mechanisms
a, Schematic of the OEC showing suggested locations of ammonia binding upon illumination. **b,** Electron density in the vicinity of Mn4, showing waters W1 and W2 and their surroundings in the 2F and 2F-NH$_3$ data. (left, right) Schematic of the bonding geometry of W1 and W2 in ref[7] and the 2F and 2F-NH$_3$ RT structures; note that the 2F-NH$_3$ W2 position is not well defined and angles and distances are only approximations. **c,** Proposed O-O bond formation mechanisms; (i) Water-nucleophilic attack of Ca-bound W3 onto W2 (e.g. Mn(V)-oxo in S$_4$), (ii) coupling between W1 and O5, (iii) Oxo-oxyl radical coupling mechanism between a hydroxo bound in the S$_2$→S$_3$ transition (hydroxyl in S$_4$) to Mn1 and the O5-bridge, (iv) nucleophilic attack of Ca-bound W3 onto O5, and (v) oxo-oxyl coupling between W1 and O4.